RESEARCH ARTICLE

PLP2 drives collective cell migration via ZO-1-mediated cytoskeletal remodeling at the leading edge in human colorectal cancer cells

Dipanjana Ghosh[1,2,*], Ankita Dutta[1], Anjali Kashyap[1], Neeraj Upmanyu[2] and Sunando Datta[1,*]

ABSTRACT

Collective cell migration (CCM), in which cell–cell integrity remains preserved during movement, plays an important role in the progression of cancer. However, studies describing CCM in cancer progression are majorly focused on the effects of extracellular tissue components on moving cell plasticity. The molecular and cellular mechanisms of CCM during cancer progression remain poorly explored. Here, we report that proteolipid protein 2 (PLP2), a colonic epithelium-enriched transmembrane protein, plays a vital role in the CCM of invasive human colorectal cancer (CRC) epithelium by modulating leading-edge cell dynamics in 2D. The extracellular pool of PLP2, secreted via exosomes, was also found to contribute to the event. During CCM, the protein was found to exist in association with ZO-1 (also known as TJP1) and to be involved in the positioning of the latter at the migrating edge. PLP2-mediated positioning of ZO-1 at the leading edge further alters actin cytoskeletal organization that involves Rac1 activation. Taken together, our findings demonstrate that PLP2, via its association with ZO-1, drives CCM in CRC epithelium by modulating the leading-edge actin cytoskeleton, thereby opening up new avenues of cancer research.

This article has an associated First Person interview with the first author of the paper.

INTRODUCTION

In collective cell migration (CCM), a group of cells moves together as a single unit while maintaining their cell–cell contacts, coordinating cytoskeletal dynamics, intercellular communication (Ilina and Friedl, 2009) and a collective front–rear polarity (Haeger et al., 2015). The front consists of leader cells that sense the external environment and drive the collective movement by guiding the entire layer for speed and directionality. Cells at the rear end of the cluster are termed as the followers, which remain connected to the leaders through cell–cell contacts, and thus maintain intercellular communications with the leaders and contribute to

the efficiency of the collective movement (Mayor and Etienne-Manneville, 2016). Molecular machineries at the leaders majorly include small GTPases of the Rho family, which contribute to the protrusion formation and cytoskeletal rearrangement (Mayor and Etienne-Manneville, 2016), and integrin, which contributes to leader-cell polarization (Yamaguchi et al., 2015). At the follower end, protein molecules involved in focal adhesion, adherens junctions and tight junctions (TJs) undergo force-induced conformational changes and thereby govern transmission of information from the leader to the followers through mechanosensing (Das et al., 2015; Hegerfeldt et al., 2002; Matsuzawa et al., 2018; Peglion et al., 2014; Plutoni et al., 2016).

CCM plays a major role during organ development, tissue regeneration and cancer progression (Friedl and Gilmour, 2009). In the context of epithelial cancer progression, CCM is mainly being studied in 3D invasion models to explore the plasticity of the cancer cells moving through the extracellular matrix components (Friedl et al., 1995, 2012; Ladoux and Mège, 2017; Hegerfeldt et al., 2002). However, the underlying molecular and cellular mechanisms of the CCM during cancer progression remain poorly explored. Here, we uncover the role of a transmembrane protein, proteolipid protein 2 (PLP2) (Breitwieser et al., 1997; Oliva et al., 1993), in the CCM of a colon cancer cell type in which epithelial–mesenchymal transition (EMT) has been triggered (Kim et al., 2013; Warburton et al., 1992; Yoon et al., 2008). PLP2 was first discovered as a colonic epithelium-enriched protein in a highly differentiated colon cancer cell line and was found to possess an expression gradient along the colonic crypt in normal individuals (Oliva et al., 1993). Latter studies have reported its role in the progression of several other cancer types (Chen et al., 2018; Feng et al., 2020; Ozawa et al., 2012; Son et al., 2004; Sonoda et al., 2010). However, the underlying mechanism by which PLP2 drives the progression of colorectal cancer (CRC) remained elusive. The current study demonstrates that PLP2 plays a vital role in CCM of colon cancer epithelium and further investigates the underlying molecular mechanism. Zonula occludens-1 (ZO-1; also known as TJP1), a TJ scaffold protein, was found to associate with PLP2 through the cytoplasmic C-terminus of the latter. This association was found to be essential for ZO-1 positioning to the leading edge, thereby driving CCM through reorganization of the actin cytoskeleton at the leading cell population.

RESULTS

PLP2 shows dynamic membrane localization in colon cancer epithelium

To begin with, we compared the levels of endogenous PLP2 expression amongst the CRC cell lines of epithelial (Caco-2) (Hashimoto and Shimizu, 1993; Kim et al., 2013) and invasive epithelial (SW480) (Kim et al., 2013; Warburton et al., 1992; Yoon et al., 2008) origin. Endogenous PLP2 expression was significantly

[1]Department of Biological Sciences, Indian Institute of Science Education and Research, Bhopal 462066, India. [2]School of Pharmacy and Research, People's University, Bhopal 462037, India.

*Authors for correspondence (sunando@iiserb.ac.in; dghosh@iiserb.ac.in; dipanjanagh@gmail.com)

D.G., 0000-0003-0887-6798; A.D., 0000-0001-9624-0305; A.K., 0000-0002-8955-5381; N.U., 0000-0001-9289-8492; S.D., 0000-0002-1417-0276

higher in the SW480 cell line at both the RNA and protein level (Fig. S1A,B). Therefore, we selected SW480 cells to study the possible cellular role of PLP2 in CRC advancement. The SW480 cell line was reported to be highly malignant in nature and accordingly shows efficient migration while maintaining partial epithelial characteristics (Berger et al., 2010; Warburton et al., 1992). Before proceeding, we confirmed its migratory and epithelial characteristics by probing against several markers for both the features. In low-density culture, this cell line forms lamellipodia-like (Wilson et al., 2013) actin-rich membrane protrusions at the free edge, as evident from F-actin staining (Fig. S1C,C′). In high-density culture, the cell line partially preserves the epithelial characteristics (Fig. S1C,C′), as evident from the localization of cell–cell junction (CCJ)-associated proteins, ZO-1 (61% cells) and occludin (45% cells) (Fig. S1D–E′).

One of the major determinants of the cellular function of a protein molecule is its subcellular localization (Loo et al., 2014). In low-density cultures, PLP2 was found to localize at the free-edge membrane protrusions (Fig. 1Aa), whereas in dense culture it localizes to the CCJ (Fig. 1Ad). The protein was also present at intracellular puncta (Fig. 1A, pink arrowheads). Expression of PLP2 with C-terminal GFP or mCherry tags showed identical localization (Fig. 1Ab,c,e,f). At the free-edge membrane protrusions, PLP2-GFP colocalizes with F-actin (Fig. 1B–B″) and a cortical actin-binding protein cortactin (Fig. 1B–B″). The extent of colocalization is comparable to that between cortactin and F-actin (Fig. 1B–B″). At the CCJ, it colocalizes with TJ scaffold ZO-1 (Fig. 1C–C″). We further characterized the punctate localization of PLP2 based on an earlier report (Timms et al., 2013) in which PLP2 was described as an endosomal resident protein in epithelial cells. In corroboration, we also observed that ∼17% of PLP2-GFP colocalized with the early endosomal marker EEA1, suggesting the presence of PLP2-GFP in the endosomal pool (Fig. S1F, top row). Moreover, in earlier proteomics studies, PLP2 was enlisted as an exosomal cargo, secreted from several types of cancer cells, including SW480 (Hurwitz et al., 2016; Ji et al., 2013). We therefore tested the colocalization of PLP2 or PLP2-GFP with the exosomal marker CD63 (Andreu and María, 2014) (Fig. 1D,D′; Fig. S1F, top row). It was observed that PLP2 (or PLP2-GFP) colocalized with CD63 on the vesicles that were predominantly located at the perinuclear region, although some of them were also located away from the perinuclear zone (Fig. 1D; Fig. S1F, zoomed insets). The CD63-positive perinuclear vesicles of PLP2 may possibly represent the mature endocytic compartments, part of which will eventually fuse with the plasma membrane to release exosomes (Bobrie et al., 2011; Colombo et al., 2014; Hurwitz et al., 2017; Park et al., 2018; Verweij et al., 2011). A small fraction of vesicular PLP2-GFP also colocalized with Rab27a, which regulates exosome secretion (Ostrowski et al., 2010) (Fig. S1F, bottom row). We then isolated density gradient-purified exosomes from SW480 and the cells stably overexpressing PLP2-GFP. The exosomes obtained from SW480 and PLP2-GFP cells were named as 'exosome^SW480' and 'exosome^PLP2-GFP', respectively. Enrichment of PLP2 or PLP2-GFP in isolated exosome preparations further confirmed it as an exosomal cargo (Fig. S1G–H). The exosomes purified from SW480 cells were further characterized for their shape and size distribution using nanoparticle tracking analysis (NTA) (Fig. S1G′) and transmission electron microscopy (TEM) (Fig. S1G″).

Taken together, these data suggest that PLP2 exists in distinct intracellular and extracellular pools in colon cancer epithelium cells. The intracellular pool is distributed among membrane protrusions, CCJs and intracellular vesicles (Fig. 1B–D′; Fig. S1F,I, Movie 1), while the extracellular pool is secreted via exosomes (Fig. S1G,H).

PLP2 depletion leads to abrogation in leading-edge cell dynamics during CCM

PLP2 was found to localize at the actin-rich membrane protrusions as well as CCJs in our study (Fig. 1; Movie 1). The localization of PLP2 at the actin-rich membrane protrusions indicates its possible involvement in cell motility (Wilson et al., 2013), whereas its localization to the CCJs indicates its possible role in maintaining cell–cell integrity (Lee, 2015). A balance between these two events is the key to CCM (Friedl and Mayor, 2017; Ilina and Friedl, 2009). Therefore, we proceeded to investigate the possible involvement of PLP2 in CCM. At first, we monitored CCM in the wild-type SW480 cell line (Movie 2) and then followed PLP2 localization in SW480 cells during CCM. A confluent monolayer of the cells stably expressing PLP2-GFP or co-expressing PLP2-GFP and mCherry-cortactin was scratch wounded and allowed to migrate in 2D (Grada et al., 2017). Time-lapse imaging was carried out using confocal microscopy to follow the localization of the ectopically expressed proteins during CCM. PLP2-GFP showed a dynamic localization between the CCJs and the protrusions at the migrating edges (Fig. 2A; Movie 3). Moreover, PLP2-GFP at the migrating edges colocalized with mCherry-cortactin (Fig. 2B; Movie 4), a leading-edge marker (Weed et al., 2000).

To further investigate whether PLP2 has any role in CCM, we studied collective migration in PLP2-depleted cells (Movie 5). ON-TARGETplus SMARTpool siRNA against PLP2 was used to downregulate PLP2 expression (Fig. S2A,A′). PLP2-depleted cells were then subjected to wound creation, and the wound closure was followed for 12 h by live-cell video microscopy. Observed CCM was compared with that of the cells treated with non-targeted SMARTpool siRNA, denoted as the Scr control cells. To obtain a collective measure of the migration parameters of the cells, we carried out particle image velocimetry (PIV) analysis, a whole-field cross-correlation technique that provides local displacements in real time for the entire cell monolayer (Petitjean et al., 2010; Vig et al., 2016). The velocity field revealed the presence of multiple high-speed zones at the wound front or leading edge of the Scr control cells (Fig. S2B). PLP2-depleted cells showed a significant reduction in the number of these high-speed zones and average collective speed obtained from the PIV analysis (Fig. S2B,C). Moreover, to further quantify the migration characteristics at the leading edge, we tracked individual cells from the first four to six layers facing the wound and analyzed the speed and persistence (net displacement/total displacement) for each track or cell. The average track speed and persistence were found to be significantly reduced in PLP2-depleted cells (Fig. S2D,E).

To further reinforce the functional insight and rule out off-target effects, if any occurred due to the use of SMARTpool siRNA, we established a stable CRISPR-mediated PLP2 knockout clone of the SW480 cell line (PLP2KO) (Fig. S2F). PLP2KO cells exhibited perturbed cell–cell integrity, as assessed by the measurement of paracellular flux (Balda et al., 1996) (Fig. S2H); however, no effect on cell proliferation was observed (Fig. S2G). Further sets of investigations to establish PLP2 involvement in CCM were carried out in PLP2KO cells.

A combination of live-cell video microscopy, followed by PIV, individual cell tracking and computational analysis, was used to characterize cellular dynamics during 0–12 h post-wound creation. PLP2KO cells showed a delayed wound closure or slower movement, which could be rescued when PLP2-mCherry was overexpressed in PLP2KO cells (Fig. S2I, Movie 6). PIV analysis (Petitjean et al., 2010; Vig et al., 2016) revealed that the number of high-speed zones at the wound front and the average collective speed were significantly reduced in PLP2KO cells, and that they could be rescued by the
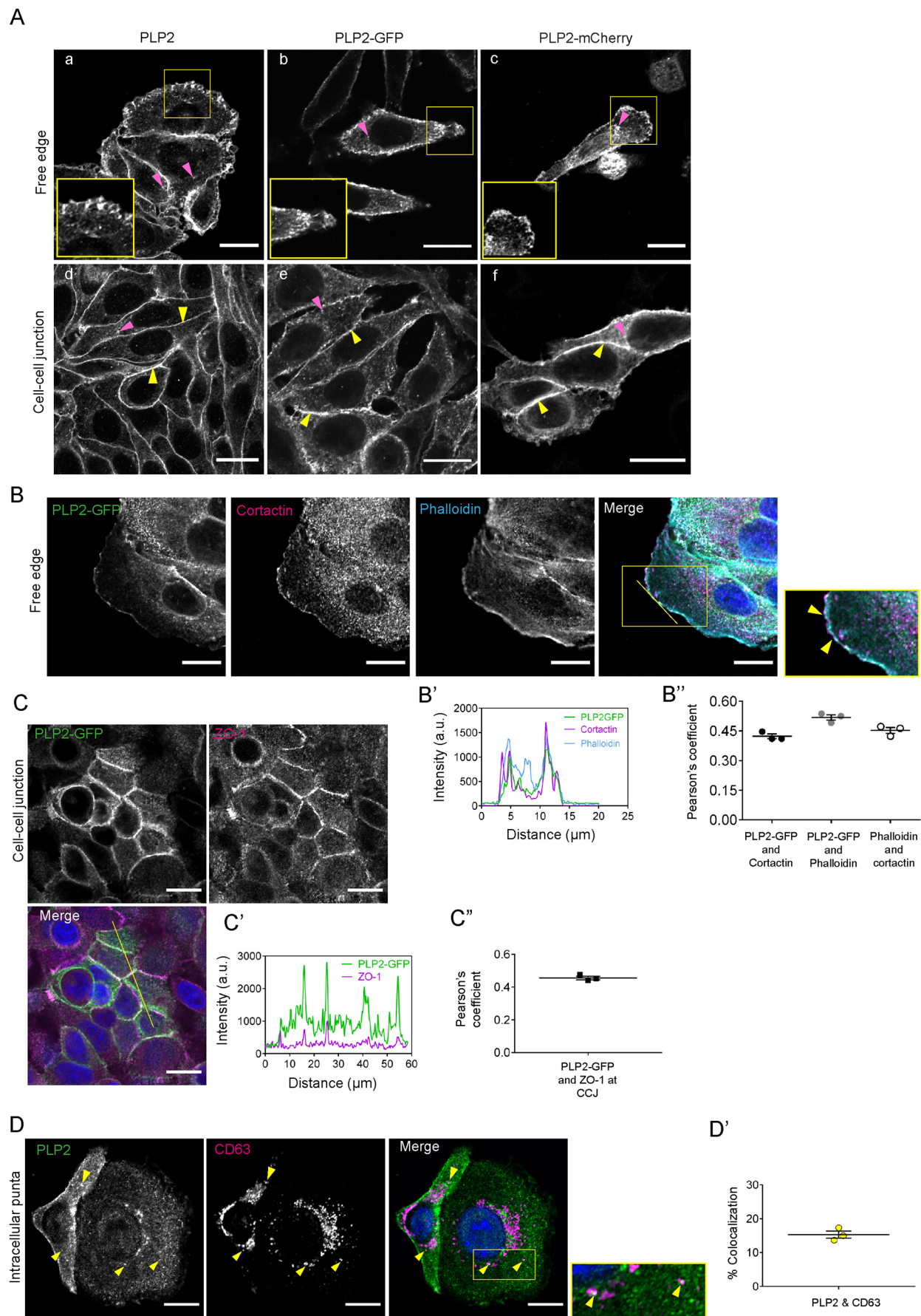
Fig. 1. See next page for legend.

Fig. 1. PLP2 shows membrane localization in an epithelial colorectal cancer cell line. (A) Endogenous PLP2 (a,d), PLP2-GFP (b,e) and PLP2-mCherry (c,f) localize to the (a–c) free-edge membrane protrusions and (d–f)cell–cell junctions (CCJs; pointed at by yellow arrowheads). Pink arrowheads indicate PLP2 localization in the intracellular puncta. (B) At the free edge, PLP2-GFP colocalizes with cortactin and F-actin. (B′) The intensity profile plot over the yellow line at the free edge in B represents the overlap amongst PLP2-GFP, cortactin and F-actin. (B″) The quantification of colocalization based on Pearson's correlation coefficient amongst PLP2-GFP, cortactin and F-actin ($n=111$, $N=3$), (C) At the CCJs, PLP2-GFP colocalizes with ZO-1. (C′) Intensity profile over the yellow line in C. (C″) Colocalization between PLP2-GFP and ZO-1 ($n=118$, $N=3$). (D) At the intracellular vesicles, PLP2 colocalizes partly with CD63 (indicated by yellow arrowheads). (D′) Object-based colocalization ($15.32\pm0.013\%$) (refer to 'Confocal image analysis' section of the Materials and Methods) of the vesicular pool of PLP2 with the exosomal marker CD63 ($n=2349$, $N=3$). Data are presented as mean±s.e.m.; n=number of cells, N=number of independent experiments. Scale bars: 15 µm; insets are zoomed images of the yellow outlined regions. a.u., arbitrary units.

overexpression of PLP2-mCherry or treatment with exosome[PLP2-GFP] (Fig. 3A–C). The role of exosomal PLP2 in CCM was further confirmed by comparing the effects observed upon treatment of PLP2KO cells with exosome[SW480] or exosome[PLP2KO] (Fig. S3B–H, Movie 7). Exosome[PLP2KO] represents exosome pools purified from the secretome of PLP2KO cells (Fig. S3C). To further confirm the effect of exosomal PLP2 on CCM, we specifically inhibited the biogenesis of exosomes in SW480 cells by treating them with GW4869 (Fig. S3B), which inhibits ceramide-dependent exosome production (Trajkovic et al., 2008). The treatment resulted in a modest reduction of PLP2 in the total exosome pool (Fig. S3A) without altering its endogenous level (Fig. S3A′), suggesting that PLP2 may be preferentially secreted through ceramide-dependent exosomes. However, the modest reduction of PLP2 levels in exosomes could possibly be caused by a compensatory effect (Palmulli and van Niel, 2018), owing to which PLP2 is packaged and secreted through the available non-ceramide dependent exosomes under GW4869 treatment. Drug-treated cells showed partial abrogation of CCM, as evident from their diminished speed and marginally altered persistence (Movie 8, Fig. S3I–M). However, the detailed underlying mechanism of how exosomal PLP2 contributes to CCM is subject to further investigation.

To better understand the dynamics of CCM, we further computed the kymographs of horizontal velocity component ('u') and local order parameter ['s' or $<\mathrm{Cos}(\theta)>$] (Fig. S2J,J′) for the control, PLP2KO and PLP2–mCherry-overexpressing PLP2KO cells. Speed, horizontal velocity and direction of migration are some of the crucial parameters impacting the dynamics of collective cell movement (Zhang et al., 2017a). The local order parameter provides a measure of the relative orientation of neighboring cells with respect to the wound during coordinated movement. The value of this parameter ranges between −1 to +1, where +1 represents collective movement perpendicular to the wound-border or towards +X (refer to Fig. 3A), and −1 represents a collective movement towards −X (Petitjean et al., 2010; Zhang et al., 2017a). As evident from both sets of kymographs, the region within 400 pixels (≈230 µm) from the wound showed active dynamics of migration parameters, and we named it the 'active zone'. Because depletion of PLP2 led to a drastic reduction in the absolute values of both u and s, whether PLP2 depletion affects the length of the active zone remains inconclusive. To understand the time dependence of these parameters, we chose an X section within the active zone and plotted u or the local order parameter, s, against time at this particular X. As shown in respective kymographs (Fig. S2Ja–c),

u steadily decayed with time, with a small hump in the initial phase for the control cells (Fig. S2J′a). The depletion of PLP2 led to a drastic reduction in u as well as much quicker decay of u with time (Fig. S2J′a). Overexpression of PLP2-mCherry in PLP2KO cells partially reverted the kymograph pattern showing partial rescue in the speed dynamics (Fig. S2J′a). In contrast, the local order parameter showed much slower decay for the control cells (Fig. S2Jd,J′b). In PLP2KO cells, the overall value of the parameter was much lower compared to that of the control cells and showed almost no dependence on time (Fig. S2Je,J′b). Overexpression of PLP2-mCherry partially increased the overall local order and rescued the decay pattern (Fig. S2Jf,J′b).

During CCM, leader cells located at the front play a major role in the collective movement (Mayor and Etienne-Manneville, 2016; Poujade et al., 2007). Hence, to further quantify the migration characteristics at the leading edge, we tracked individual cells from the first four to six layers and analyzed the speed, persistence and trajectory angles of the individual tracks over 0–12 h post-wound (Fig. 3D–H′). We observed that 70–80% of wound closure takes place between 1 h and 7 h post-wound (Fig. S2I, Movie 6); therefore, we calculated the migration parameters within this time window. The average speed (v) and persistence of the migrating cells showed a significant decrease in PLP2KO cells, which could be rescued by overexpressing PLP2-mCherry or treating the cells with exosome[PLP2-GFP] (Fig. 3D–G; Fig. S3G–H). In addition, wider trajectory angle distribution for the PLP2KO cells revealed that PLP2 depletion leads to cell migration in diverse directions (Fig. 3H,H′).

Taken together, these data suggest that, during CCM, PLP2 showed a dynamic localization between the CCJs and the wound edge (Fig. 2; Movies 3 and 4) and controls the dynamics of both speed and direction of the leading-edge cells (Fig. 3; Figs S2 and S3). Both the intracellular and exosomal pool of PLP2 contribute to this function (Fig. 3; Figs S2 and S3).

ZO-1 positioning to the cell periphery is reliant on its association with the C-terminal cytosolic tail of PLP2

To investigate the underlying molecular mechanism of PLP2-mediated CCM, we focused on the proteins that could possibly associate with PLP2 in a cellular environment. Like PLP2 (Fig. 2; Movies 3 and 4), the TJ scaffold protein ZO-1 was also reported to relocate from CCJs to the migrating edge, and has been implicated in the migration of breast epithelial monolayer, fibroblast and lung cancer cells (González-Tarragó et al., 2017; Taliana et al., 2005; Tuomi et al., 2009). It has also been shown to interact with α5β1 integrin at the lamellae structures of migrating cells (Tuomi et al., 2009). We observed that PLP2-GFP and ZO-1 colocalize at the free-edge protrusions as well as CCJs (Fig. S4A–A″) in colon cancer epithelium.

We, therefore, asked whether the colocalization of PLP2-GFP and ZO-1 shows any particular dynamics during wound closure. PLP2-GFP and ZO-1 were found to colocalize at the wound edge in the early hours (0 h and 4 h) of CCM (Fig. 4Aa,b,B; Fig. S7A). At 4 h post-wound, notable umbrella-like extensions (Fig. 4A,b and insets) were observed at the migrating edges, and the two proteins were found to be largely colocalized at the boundary of these structures. In contrast, PLP2-GFP and ZO-1 colocalization at CCJs was largely dropped during the initial 4 h post-wound (Fig. 4Ab,B; Fig. S7A). We further asked whether these two proteins show co-dynamics at the leading edge of the migrating cells. Time-lapse confocal microscopy of the migrating cells overexpressing PLP2-mCherry and ZO-1-mEmerald was carried out to study the co-dynamics at the leading edge (Movie 9). At 16 h, they colocalized mostly at the CCJs and not at the wound edge. The disappearance of umbrella-like structures was
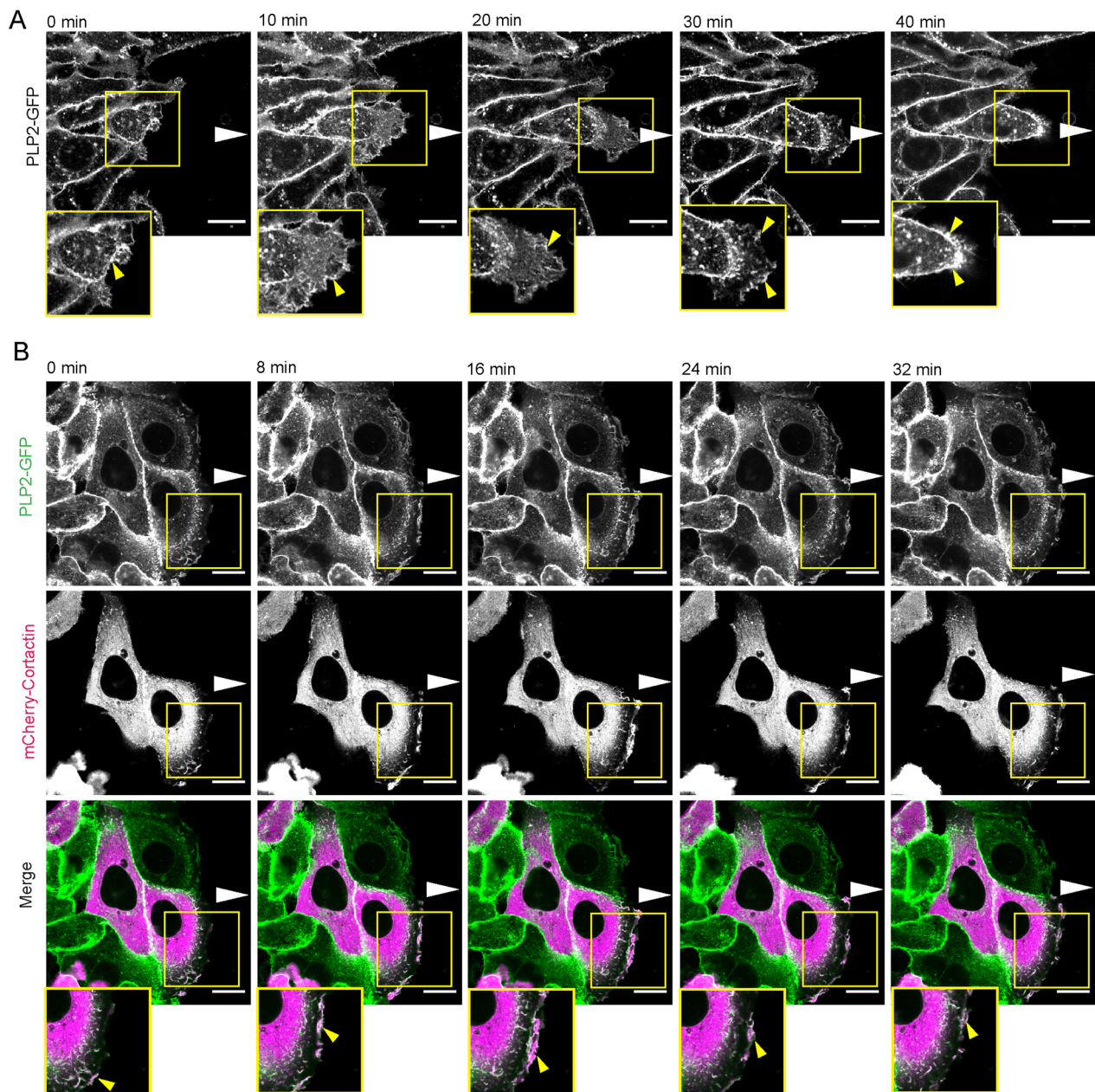
Fig. 2. PLP2-GFP localizes to the leading edge during collective cell migration (CCM). (A) Time-lapse confocal images of PLP2-GFP during migration (2 h post-wound). (B) PLP2-GFP colocalizes with mCherry-cortactin at the leading edge during CCM (4 h post-wound). Scale bars: 15 µm; insets are zoomed images of the yellow outlined regions. White arrowheads indicate the direction of migration; yellow arrowheads indicate co-dynamics of PLP2-GFP and mCherry-cortactin at the migrating edges.

also evident at this hour (Fig. 4Ac,B; Fig. S7A). This colocalization pattern directed our focus towards exploring a possible intracellular association between PLP2 and ZO-1.

It has been reported that the MARVEL domain-containing proteins (Raleigh et al., 2010; Sánchez-Pulido et al., 2002), including occludin (Furuse et al., 1994) and tricellulin (Riazuddin et al., 2006), interact with ZO-1. To investigate whether PLP2, a MARVEL domain-containing protein (Breitwieser et al., 1997), exists in association with ZO-1 in the cellular context, we used a modified nanobody pull-down approach (Rothbauer et al., 2006, 2008; Tang et al., 2013). GST-tagged GFP-binding protein (GBP) or Cherry-binding protein (CBP) was used to pull down GFP- or mCherry-tagged PLP2 protein from the respective cell lysates. In

both cases, ZO-1 was co-eluted (Fig. 4C; Fig. S4B) with GFP- or mCherry-tagged PLP2, suggesting an intracellular association between PLP2 and ZO-1.

We then went on to delineate the particular region of PLP2 that associates with ZO-1. ZO-1, a peripheral membrane protein acting as a junctional scaffold in polarized epithelial cells (Tornavaca et al., 2015), interacts with multiple transmembrane proteins (Ebnet et al., 2000; Furuse et al., 1994; Itoh et al., 1999) that are likely to associate with ZO-1 through their cytoplasmic ends, as observed for occludin (Furuse et al., 1994) and tricellulin (Riazuddin et al., 2006). In order to delineate whether ZO-1 associates with PLP2 via the latter's N-terminal or C-terminal cytosolic region, we created two deletion varieties of PLP2 – ΔNPLP2 and PLP2ΔC – by removing the
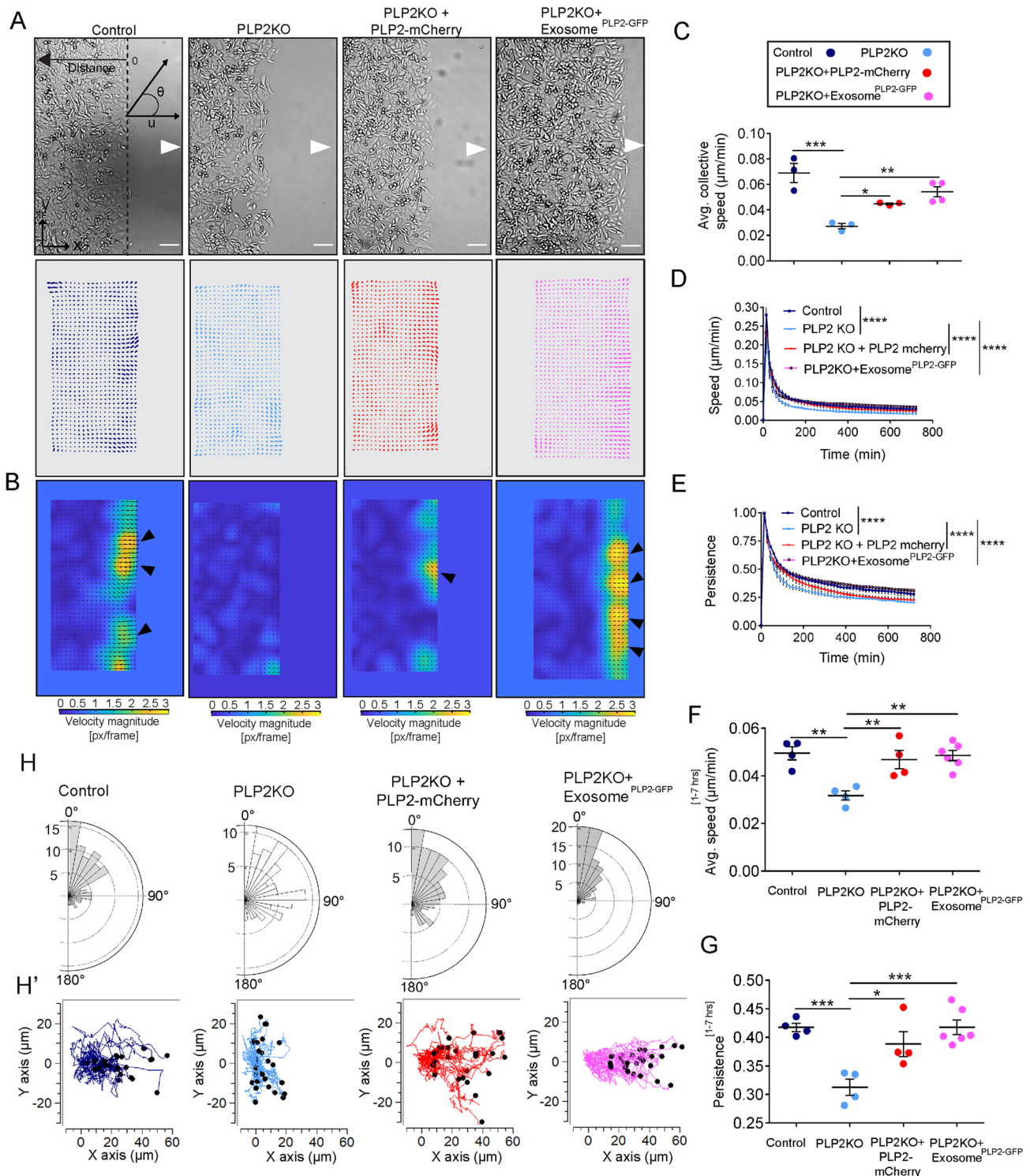
Fig. 3. PLP2 plays a crucial role in CCM. (A–H′) Wound scratch assay performed on control, PLP2KO and PLP2KO cells overexpressing PLP2-mCherry or treated with exosome[PLP2-GFP]. (A–C) PIV analysis. (A) Phase-contrast images and corresponding velocity fields 7 h post-wound. White arrowheads indicate the direction of migration. (B) Velocity heatmaps (1 pixel=0.586 μm; one frame=15 min; high-speed zones, yellow regions pointed at by black arrowheads). (C) Average collective speed measured between 1 h and 7 h post-wound from three independent experiments for control, PLP2KO and PLP2KO+PLP2-mCherry (N=3) and four independent experiments for PLP2KO+exosome[PLP2-GFP] (N=4). (D–H′) Track analysis. Individual cells are tracked from the first four layers of the progressing cell sheet. (D,E) Speed (D) and persistence (E) over 12 h post-wound. (F,G) Average speed (F) and persistence (G) measured between 1 h and 7 h post-wound. For D–G, n=294 for control (N=4), n=226 for PLP2KO (N=4), n=278 for PLP2KO+PLP2-mCherry (N=4), n=645 for PLP2KO+exosome[PLP2-GFP] (N=6). (H) Rose plots of trajectory angles. The magnitude of each bar shows the fraction of cells with the indicated angle trajectory. n=294 for control (N=4), n=288 for PLP2KO (N=5), n=361 for PLP2KO+PLP2-mCherry (N=5), n=519 for PLP2KO+exosome[PLP2-GFP] (N=5). (H′) Trajectories of 30 representative cells measured over 12 h. Data are presented as mean±s.e.m. for C–G; n=number of cells or tracks, N=number of experiments. Statistical significance was calculated using one-way ANOVA; *P<0.05, **P<0.005, ***P<0.0005, ****P<0.0001. Scale bars: 100 μm.

cytosolic N- or C-terminus, respectively (Fig. S4C–C″). Using the GST-CBP pull down, we observed that ΔNPLP2-mCherry could successfully pull down ZO-1, whereas mCherry–PLP2ΔC failed to pull it down (Fig. 4D), suggesting that PLP2 associates with ZO-1 through its C-terminal cytosolic region.

Since PLP2 and ZO-1 colocalized at the cell periphery (Fig. S4A–A″) and showed biochemical association (Fig. 4C,D; Fig. S4B), we hypothesized that localization of ZO-1, a peripheral membrane protein (McNeil et al., 2006), might rely on its association with PLP2, a membrane protein (Breitwieser et al., 1997). We observed that, in PLP2KO cells, ZO-1 could not localize to the free-edge membrane protrusions (Fig. 4Ea,E′a; Fig. S7B) or CCJs (Fig. 4Eb,E′b). Of note, ZO-1 protein levels showed a notable reduction in the PLP2-depleted cells (Fig. S4D) with unaltered mRNA levels (Fig. S4D′). However, the comparison of the normalized fluorescence intensities of peripheral ZO-1 between control and PLP2KO cells suggests that the perturbation of peripheral ZO-1 localization is not exclusively an effect of reduced ZO-1 protein levels (Fig. S4D″). Moreover, ZO-1 localization to free-edge membrane protrusions, as well as CCJs, could be rescued in PLP2KO cells overexpressing PLP2-mCherry and ΔNPLP2-mCherry but not those overexpressing mCherry-PLP2ΔC (Fig. 4E,E′; Fig. S7B). This result further confirms our hypothesis, suggesting that ZO-1 positioning to the cell periphery depends on the PLP2–ZO-1 association.

Taken together, these data indicate that ZO-1 and PLP2 exist in an association that is mediated by the C-terminal cytosolic tail of PLP2. Additionally, this association is vital for ZO-1 positioning to the cell periphery.

PLP2–ZO-1 association contributes to CCM by impacting the abundance of leading-edge actin-rich membrane protrusions

To probe whether PLP2–ZO-1 association has any implications in PLP2-mediated CCM, we first investigated ZO-1 localization during the early hours of wound closure. Previously, we have shown that, during the early hours of CCM, ZO-1 colocalizes with PLP2 at the migrating edges (Fig. 4Ab,B; Fig. S7A, Movie 9). In PLP2KO cells, ZO-1 could not localize to the leading edges, and, notably, the umbrella-like structures were also less frequently observed (Fig. 5A; Fig. S5A, Fig. S7C,C′). This localization pattern of ZO-1 could be rescued by overexpressing PLP2-mCherry or ΔNPLP2-mCherry but not by overexpressing mCherry-PLP2ΔC (Fig. 5A; Fig. S5A, Fig. S7C,C′). Thus, perturbing PLP2–ZO-1 association also abrogates ZO-1 localization at the migrating edges during CCM.

We then studied CCM in PLP2KO cells overexpressing ΔNPLP2-mCherry or mCherry-PLP2ΔC (Fig. S5B, Movie 10). PIV and individual track analysis revealed that the overexpression of ΔNPLP2-mCherry, but not mCherry-PLP2ΔC, led to significant recovery in the average speed of the leading-edge cell population compared to that in PLP2KO cells (Fig. 5B–D,E; Fig. S5C,E). Persistence was temporarily rescued in the early hours of CCM by mCherry-PLP2ΔC-overexpressing cells (Fig. 5D′; Fig. S5E′); however, it failed to sustain over time (Fig. 5E′; Fig. S5E′). Trajectory angle distribution showed an improvement in the directionality of movement in PLP2KO cells overexpressing ΔNPLP2-mCherry but not in those overexpressing mCherry-PLP2ΔC (Fig. 5F,F′). The expression of mCherry-PLP2ΔC in PLP2KO cells resulted in an increase in u during the first couple of hours post-wound creation; however, its magnitude was much less compared to that for the cells expressing ΔNPLP2-mCherry, as revealed by the respective kymographs (Fig. S5Da–c,D′a). Both ΔNPLP2-mCherry- and mCherry-PLP2ΔC-overexpressing

PLP2KO cells showed marked recovery of s during 1–5 h post-wound (Fig. S5Dd–f,D′b). These results indicate that perturbing the association between PLP2 and ZO-1 abrogates the migration characteristics of the leading-edge cells.

Because dynamic regulation of actin cytoskeleton at the leading edge of migrating cells is crucial for cell motility (Ridley et al., 1992; Zigmond, 1996), we next asked whether PLP2–ZO-1 association has any role in actin organization at the leading edge during CCM. To address this, we set out to stain the migrating cells with phalloidin to probe for umbrella-like structures at 4 h post-wound (Fig. 5G; Fig. S7D). Quantification of the confocal images revealed that F-actin-rich umbrella-like protrusions (Fig. 5G; Fig. S5F, Fig. S7D) were significantly less abundant at the migrating edges of PLP2KO cells (Fig. 5G; Fig. S5F, Fig. S7D). The abundance of these structures could be rescued by overexpressing PLP2-mCherry or ΔNPLP2-mCherry but not by overexpressing mCherry-PLP2ΔC (Fig. 5G; Fig. S5F, Fig. S7D). We also verified our observations by immunofluorescence studies using an antibody against cortactin (Weed et al., 2000) (Fig. 5H; Fig. S5G). Hence, the perturbation of PLP2–ZO-1 association affects the abundance of F-actin-rich umbrella-like structures during CCM.

Taken together, these data suggest that PLP2–ZO-1 association has a role in the leading-edge cell dynamics and actin cytoskeletal remodeling at the migrating edges during CCM.

Rac1 activation contributes to PLP2-mediated CCM

The F-actin-rich umbrella-like structures formed at the migrating edges during CCM resemble lamellipodia (Small et al., 1999), which are implicated in both single-cell migration and CCM (Ridley et al., 1992; Vedula et al., 2013). The formation of lamellipodial structures is known to depend on the activation of small GTPase Rac1 (Ridley et al., 1992). Hence, we proceeded to investigate whether Rac1 is involved in the PLP2-mediated collective migration of SW480 cells.

We began by asking whether the umbrella-like structures formed during CCM at 4 h post-wound are positive for Rac1. Cells stably expressing PLP2-mCherry were transiently transfected with GFP-wild-type Rac1 (Rac1WT) and were used to study CCM. Time-lapse confocal microscopy revealed that PLP2-mCherry and GFP-Rac1WT indeed colocalize on the umbrella-like structures during CCM (Fig. 6A; Movie 11). The above finding suggests that these Rac1-positive structures may represent lamellipodia-like extensions in our model (Ridley et al., 1992; Yamaguchi et al., 2015).

Because Rac1 activation is crucial for lamellipodia formation during single-cell migration as well as CCM (Ridley et al., 1992; Yamaguchi et al., 2015), we next assessed global Rac1 activation at 4 h post-wound using biochemical Rac1 activation assay (Meriane et al., 2002). We used GST-fused p21-binding domain (PBD) of Rac1 effector p21-activated kinase (PAK) protein to pull down the membrane-bound or activated fraction of Rac1 from the whole-cell lysates of control and PLP2KO cells. As analyzed by western blotting, a marked reduction in global Rac1 activation was observed in PLP2KO cells compared to the control cells (Fig. 6B,B″; Fig. S6B,B″). PLP2KO cells overexpressing PLP2-mCherry or ΔNPLP2-mCherry showed notable recovery in the global Rac1 activation (Fig. 6B′,B″; Fig. S6B′,B″). Overexpression of mCherry-PLP2ΔC also recovered a substantial population of active Rac1, however marginally less (Fig. 6B″) than that of cells overexpressing PLP2-mCherry or ΔNPLP2-mCherry (Fig. 6B′,B″; Fig. S6B′,B″). Thus, PLP2 is playing an important role in Rac1 activation during CCM. In addition, perturbation of PLP2–ZO-1 association does not lead to complete loss of Rac1 activation.
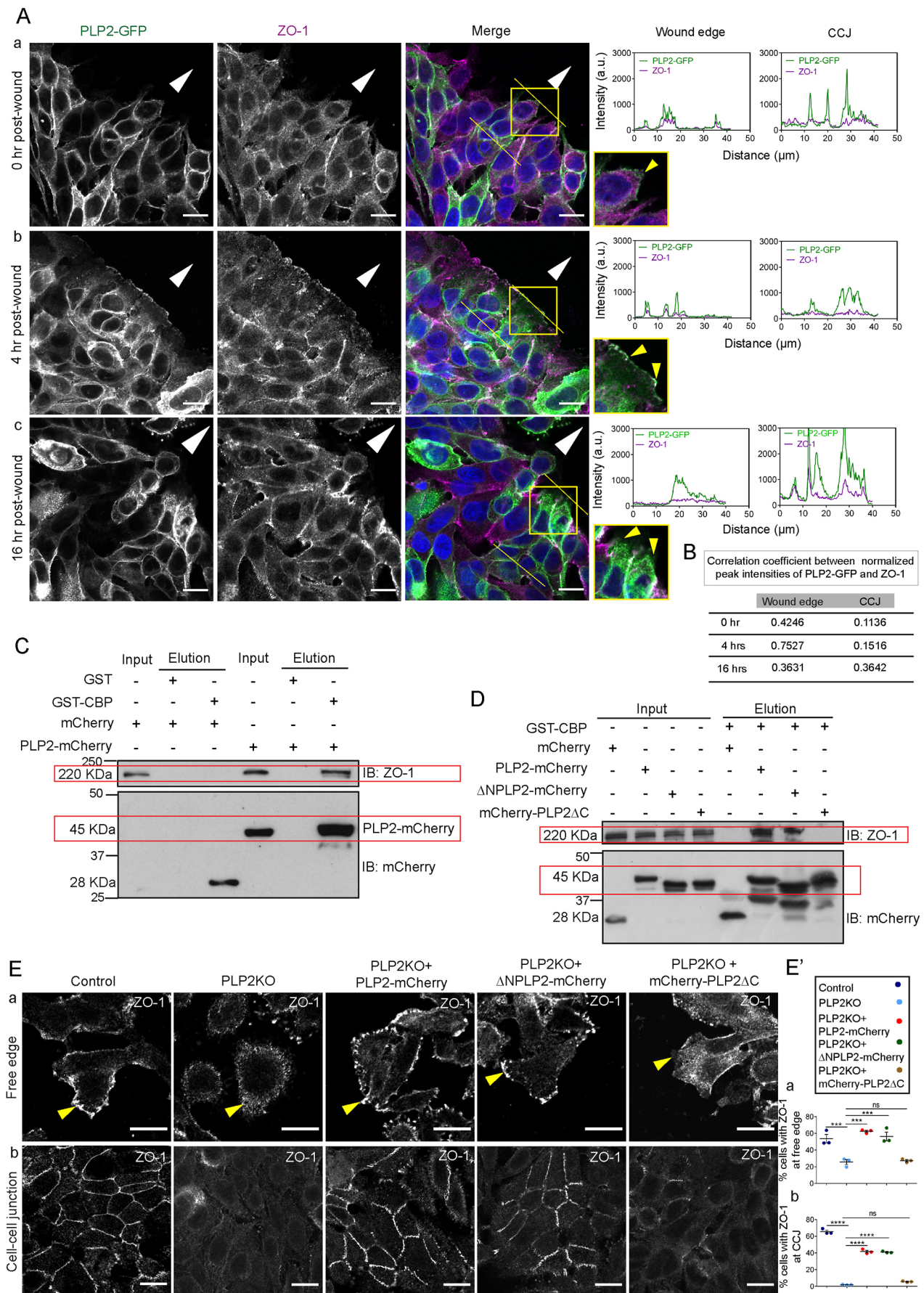
Fig. 4. See next page for legend.

Fig. 4. ZO-1 positioning to the cell periphery is reliant on PLP2–ZO-1 association. (A) Spatiotemporal colocalization of PLP2-GFP and ZO-1 at (a) 0 h, (b) 4 h and (c) 16 h post-wound; insets are zoomed images of the yellow outlined regions. The intensity plots of the fluorescence intensity (*y*-axis) against distance (*x*-axis) represent the overlap between channels. (B) Correlation between the normalized peak intensities of PLP2-GFP and ZO-1 at the wound edge as well as CCJs (data normalized with mean intensities of respective channels). Data are presented as absolute values of a correlation coefficient calculated for 240 (0 h edge), 240 (0 h CCJs), 218 (4 h edge), 240 (4 h CCJs), 225 (16 h edge) and 206 (16 h CCJs) sets of peaks from three independent experiments. (C,D) Cherry-binding protein (CBP) pull-down assay (modified immunoprecipitation approach): cleared lysates from SW480 cells overexpressing mCherry, PLP2-mCherry (C,D), ΔNPLP2-mCherry, and mCherry-PLP2ΔC (D) were incubated with GST or GST-CBP bound to glutathione-coupled agarose beads for 2 h. Beads were then washed three times with 1× PBS. The bound proteins were eluted from the beads by addition of SDS sample loading buffer, resolved by 8% SDS-PAGE and immunoblotted using anti-ZO-1 antibody (upper lanes) and anti-mCherry antibody (lower lanes). 10% of the whole-cell lysates was used as inputs. (E) ZO-1 localization at the (a) free edge and (b) CCJs. (E′) Framewise percentages of cells with ZO-1 at the (a) free edge (*n*=1433 for control; *n*=1155 for PLP2KO; *n*=910 for PLP2KO+PLP2-mCherry; *n*=668 for PLP2KO+ΔNPLP2-mCherry; *n*=797 for PLP2KO+mCherry-PLP2ΔC; *N*=3) and (b) CCJs (*n*=3184 for control; 1599 for PLP2KO; *n*=1639 for PLP2KO+PLP2-mCherry; *n*=1926 for PLP2KO+ΔNPLP2-mCherry; *n*=1757 for PLP2KO+mCherry-PLP2ΔC; *N*=3). Data are presented as mean±s.e.m. for E′; *n*=total number of cells quantified, *N*=number of independent experiments. Statistical significance was calculated using one-way ANOVA; ns, non-significant; ***P<0.0005; ****P<0.0001. Scale bars: 15 μm. White arrowheads indicate the direction of migration; yellow arrowheads indicate (A) colocalization of ZO-1 and PLP2-GFP and (E) localization of ZO-1 at the free edge.

To further investigate whether Rac1 activity is important during PLP2-mediated CCM, we co-expressed the dominant-negative mutant of Rac1 (GFP-Rac1DN) (Foster et al., 1996; Nobes et al., 1998) with PLP2-mCherry in PLP2KO cells and studied the rescue of the number of the lamellipodia-like structures. Co-expression of GFP or GFP-Rac1WT with PLP2-mCherry was used as controls for this study. In the GFP-Rac1DN background, PLP2-mCherry could not significantly rescue the number of F-actin-rich lamellipodia-like structures (Fig. 6Cb,C′; Fig. S6Ab) compared to that of GFP or GFP-Rac1WT background (Fig. 6Ca,c,C′; Fig. S6Aa,c). Next, to address whether the PLP2-mediated CCM at the leading edge is reliant on Rac1 activation, we studied CCM in the PLP2KO cells co-expressing PLP2-mCherry and GFP, GFP-Rac1DN or GFP-Rac1WT (Fig. 6D–H; Fig. S6C–F, Movie 12). PIV and track analysis revealed that the co-expression of PLP2-mCherry and GFP-Rac1DN failed to rescue the number of leading-edge high-speed zones (Fig. 6D), average collective speed (Fig. 6D′; Fig. S6D), average track speed (Fig. 6E; Fig. S6E), persistence (Fig. 6F; Fig. S6F) and trajectory angle distribution (Fig. 6G,H).

Taken together, these results suggest that PLP2-mediated CCM involves Rac1 activity at the leading edge.

DISCUSSION

Collective cell behavior relies upon intercellular coordination and junctional stability (Friedl and Mayor, 2017). While migrating as collectives, cells maintain a dynamic range of cell–cell couplings depending on the cell type (Friedl and Mayor, 2017; Scarpa et al., 2015). Epithelial cancer cells, upon EMT initiation, exhibit partial epithelial features, remain loosely attached to each other and uphold a flexible cell–cell adhesion system (Jolly, 2015; Nieto et al., 2016; Theveneau and Mayor, 2011). This type of cell closely demonstrates typical collective migration categorized as 'moving cell networks', in which the cells sense the external cues and migrate collectively

with a variable tendency to individualize (Haeger et al., 2014; Ilina et al., 2011; Theveneau and Mayor, 2011). Cancer cells with more epithelial features like Caco-2 exhibit a 'moving sheets' type of CCM, in which cells remain tightly coupled to each other during migration (Friedl and Mayor, 2017; Peyret et al., 2019).

Our study is designed on a CRC cell line of epithelial origin in which EMT has been initiated (Kim et al., 2013; Warburton et al., 1992; Yoon et al., 2008). Because EMT represents one of the hallmarks of metastasis (Nieto et al., 2016), this cell type with partial epithelial features represents an appropriate model for studying CRC advancement (Yoon et al., 2008). As collectives, the cell type was found to migrate actively during the first 7 h post-wound (Fig. S2I, Movies 2 and 6). Excluding the initial stochasticity induced by wound creation, 1–7 h post-wound was considered as the 'peak CCM hours'. During peak CCM hours, the cell type migrates with an average speed of ≈0.06 μm/min (Fig. 3C,F), whereas the average CCM speed for polar epithelial cells like Madin-Darby canine kidney (MDCK) cells is 0.13±0.016 μm/min (Petitjean et al., 2010) and for fibroblast-like NRK cells is ≈0.06 μm/min (Petitjean et al., 2010). The number of layers until which the horizontal component of the velocity remains largely unaltered represents a measure of collectiveness (Das et al., 2015; Petitjean et al., 2010). In the cell type used in our study, this number corresponds to ≈6–7 cell layers (≈110 μm away from the wound) (Fig. S2Ja). For MDCK cells, this length is ~200 μm, corresponding to ≈15 cells, and for NRK cells, this length is ≈40 μm, corresponding to ≈2 cells (Petitjean et al., 2010). Whereas the former represents the 'epithelial sheet migration', the latter shows a more individualized type of migration (Petitjean et al., 2010). The cell type used in our study thus represents a degree of collectiveness intermediate between the polar epithelial and the fibroblast-like cell types, which also corroborates with its partial epithelial characteristics (Fig. S1E,E′) (Yoon et al., 2008). Based on the above observations, we propose that the CCM exhibited by SW480 cells may closely represent the moving cell networks in 2D (Friedl and Mayor, 2017; Haeger et al., 2014; Ilina et al., 2011).

During CCM of this cell type, PLP2 showed a dynamic localization between leading-edge lamellipodia-like structures and CCJs, making it a potential candidate to exploit for CCM (Fig. 2; Movies 3 and 4). In the absence of PLP2, cells were found to lose their average speed and directionality during CCM, and both could be rescued significantly by overexpression of PLP2 as well as treatment with the exosomal pool of PLP2 (Fig. 3; Figs S2 and S3). Notably, the exosomal pool of PLP2 remarkably enhanced directional movement during CCM (Fig. 3H,H′), which could be an indication of enhancement of cell polarity. A similar observation was reported by Sung et al. (2015), where the authors showed that the exosomal delivery of fibronectin in an autocrine fashion promotes directional motility via fortification of cell polarization and modulation of adhesion assembly. These observations further established PLP2 as an important player in the collective behavior exerted by partial epithelial cells. During peak CCM hours, PLP2 was found to exist in association with the peripheral membrane protein ZO-1 at the leading edge (Fig. 4Ab and Fig. 7A; Fig. S4, Movie 9), whereas this association was more pronounced at the CCJs during the late hours of CCM, when the cells represent more stationary behavior (Fig. 4Ac and Fig. 7A). Of note, ZO-1 is established as a cytoskeletal adaptor at the TJs of stationary polar epithelial cells (Tornavaca et al., 2015). However, during cancer cell migration, ZO-1 is reported to be localized to the lamellipodia structures, stabilizing lamella formation in specific directions via its interaction with α5β1 integrin (González-Tarragó et al., 2017;
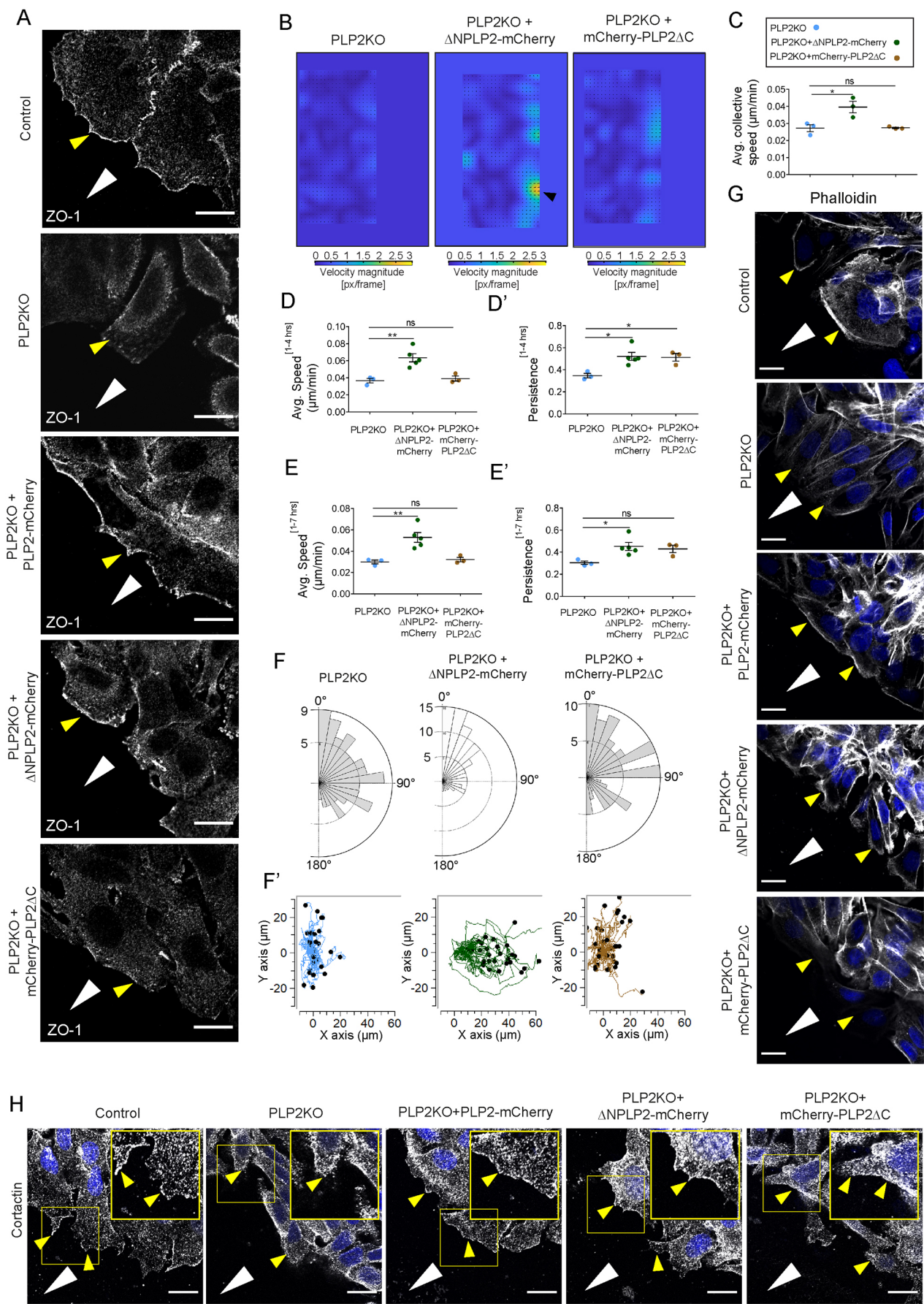
Fig. 5. See next page for legend.

Fig. 5. PLP2–ZO-1 association contributes to CCM via cytoskeletal remodeling at the leading edge. (A–H) Wound scratch assay performed on control, PLP2KO and PLP2KO cells overexpressing PLP2-mCherry, ΔNPLP2-mCherry or mCherry-PLP2ΔC in respective cases. (A) ZO-1 localization at the migrating edge at 4 h post-wound; corresponding intensity-based quantitation is shown in Fig. S5A. (B,C) PIV analysis: (B) velocity heatmaps (1 pixel=0.586 μm; one frame=15 min; high-speed zones, yellow regions pointed at by black arrowheads) and (C) average collective speed measured between 1 to 7 h post-wound from three independent experiments (N=3). (D–F′) Track analysis. (D–E′) Average speed (D,E) and persistence (D′,E′) measured between 1 h and 4 h (D,D′) and between 1 h and 7 h (E,E′) post-wound. For D and E, n=181 for PLP2KO, n=212 for PLP2KO+ΔNPLP2-mCherry and n=135 for PLP2KO+mCherry-PLP2ΔC from three, five and three independent experiments, respectively. For D′ and E′, n=175 for PLP2KO, n=212 for PLP2KO+ΔNPLP2-mCherry and n=90 for PLP2KO+mCherry-PLP2ΔC from three, five and three independent experiments, respectively. (F) Rose plots of angle trajectories. The magnitude of each bar indicates a fraction of cells with the indicated angle trajectory [n=128 for PLP2KO (N=3); n=166 for PLP2KO+ΔNPLP2-mCherry (N=3); n=107 for PLP2KO+mCherry-PLP2ΔC (N=3)]. (F′) Trajectories of 30 representative cells or tracks measured over 12 h. (G) Phalloidin staining: F-actin distribution at the migrating edges at 4 h post-wound. (H) Cortactin distribution at the migrating edges at 4 h post-wound; insets are zoomed images of the yellow outlined regions. In C–E′, data are presented as scatter plots with mean±s.e.m.; n=number of tracks or cells, N=number of independent experiments. Statistical significance was calculated using one-way ANOVA; ns, non-significant; *P<0.05, **P<0.005. White arrowheads indicate the direction of migration; yellow arrowheads indicate localization of (A) ZO-1, (G) F-actin and (H) cortactin at the migrating edges. Scale bars: 15 μm.

Taliana et al., 2005; Tuomi et al., 2009). Our results showed that ZO-1 positioning to the cell periphery is reliant on its association with PLP2 (Figs. 4E and 5A; Figs. S4D″ and S5A). The perturbation of the association abrogated the collective behavior of the cells (Fig. 5B-F′; Fig. S5B-E′), as reflected by the alteration of average speed, persistence, trajectory angle distribution and polar order parameter. However, directional movement, as represented by persistence and horizontal velocity component, was temporarily recovered during early CCM hours (1–4 h post-wound) even in the absence of this association (Fig. 5D′; Fig. S5Dc). These data indicate the involvement of other interacting partners of PLP2 that work temporarily under mechanochemical signals generated in immediate response to the wound and are associated with polarized movement (Petrie et al., 2009). In addition, actin cytoskeletal remodeling occurring at the leading edge during CCM was also found to be regulated by PLP2 and its association with ZO-1 (Fig. 5G,H; Fig. S5F,G). As a cytoskeletal adaptor, ZO-1 is known to connect the actin cytoskeleton with the membrane proteins (Fanning et al., 1998), which could possibly be one of the mechanisms underlying PLP2–ZO-1-mediated cytoskeletal remodeling at the leading edges of migrating cells. Moreover, the cytoskeletal alterations at the leading edge were found to involve Rac1 activation (Fig. 6C,C′; Fig. S6A) (Ridley et al., 1992; Yamaguchi et al., 2015). In the absence of Rac1 activation, PLP2 failed to regulate the collective behavior of the cells, as evident from the rescue experiments performed using Rac1DN (Fig. 6D–H; Fig. S6C–F). However, the overexpression of Rac1WT in this system caused a marginal delay in CCM (Fig. 6D′,E; Fig. S6E), which is probably an effect of Rac1 activation in an unpolarized manner, causing a reduction in net displacement (Pankov et al., 2005). Interestingly, the perturbation of PLP2–ZO-1 association did not markedly reduce the active Rac1 population (Fig. 6B′,B″; Fig. S6B′,B″), suggesting that the association may not have any major role in global Rac1 activation. However, the perturbation of this association led to cytoskeletal alterations at the leading edge and successive abrogation of collective migration (Fig. 5B–H; Fig. S5).

Based on these results, we propose that the association between ZO-1 and PLP2 may contribute to polarized activation of Rac1, which is important for directive cell migration during CCM. However, it would be interesting to unravel other intermediate molecular players that bridge between PLP2–ZO-1 association and Rac1 during CCM. Of note, other reports on CCM have dissected some of these bridging molecules, such as the angiomotin–Rich1 axis to connect merlin with Rac1 (Das et al., 2015) and β-PIX to connect P-cadherin with Cdc42 (Plutoni et al., 2016). Together, our results established PLP2 as one of the promising candidates for CCM of CRC epithelium closely representing moving cell networks, in which it primarily regulates the leading-edge cell dynamics via cytoskeletal remodeling (Fig. 7B).

However, before PLP2 could be established as a common CCM regulator, one needs to extend the study beyond a specific CRC cell line. Here, we utilized the loss-of-function approach in a cell line adequately expressing PLP2. A gain-of-function approach in cell line(s) like Caco-2 (Fig. S1A,B) or HT-29 (Oliva et al., 1993), which scarcely express the protein, will complement the current study. An earlier study demonstrating P-cadherin-induced intercellular mechanotransduction during CCM used a similar approach, in which C2C12 myoblasts with no endogenous expression of P-cadherin were utilized (Plutoni et al., 2016). Another degree of complexity that inevitably arises while studying CCM in multiple cell lines is the variable CCM types exhibited by different types of cancer epithelial cells. Complete epithelial CRC cells like Caco2, HT29 and HCT116 are likely to exhibit CCM of moving sheets type (Karagiannis et al., 2014; Ozawa et al., 2020; Stadler et al., 2018), whereas lymph node metastatic SW620 (Leibovitz et al., 1976) and LoVo (Aznavoorian et al., 1990) CRC cells with partial epithelial features may exhibit CCM of moving cell network type (Bozzuto et al., 2015; Stadler et al., 2018). It will therefore be interesting to investigate whether PLP2 function is limited to the CCM subtype observed here or whether it plays diverse role in multiple CCM types.

Studies focused on epithelial sheet migration in the polar epithelium and myoblast cells reported the involvement of molecular mechanotransducers like P-cadherin and merlin, which control intercellular coordination through mechanotransduction (Das et al., 2015; Plutoni et al., 2016). Although our observation on paracellular flux indicates the possible role of PLP2 in cell–cell coupling, the indirect assessment of intercellular coordination through kymograph analysis could not provide any such evidence (Fig. S2J,J′). The inconclusive spatial dynamics of the migration parameters may also be due to the drastic reduction of their absolute values upon PLP2 depletion. Alternatively, cells with better junctional stability might be a more accurate model to investigate the role of PLP2 in mechanotransduction.

CCM of cancer epithelium can lead to efficient metastasis (Cheung and Ewald, 2016), and PLP2, being a vital player of CCM in colon cancer epithelium, may thus contribute to the same. However, its pathophysiological relevance should be further validated through in vivo studies using mouse xenograft models. Our study further established that PLP2 is secreted in exosomes from this cell type, and the exosomal pool of PLP2 was also found to impact the collective behavior of the cells. Tumor-derived exosomes are reported to carry a diverse range of metastatic factors as cargo molecules that facilitate disease progression (Becker et al., 2016) through cell–cell communication (Maia et al., 2018). Few examples of the large repertoire of exosomal metastatic factors include growth factor receptors (Mu et al., 2013; Zhang et al., 2017b), integrins (Paolillo and Schinelli, 2017; Sung et al., 2015), proteases (Mu
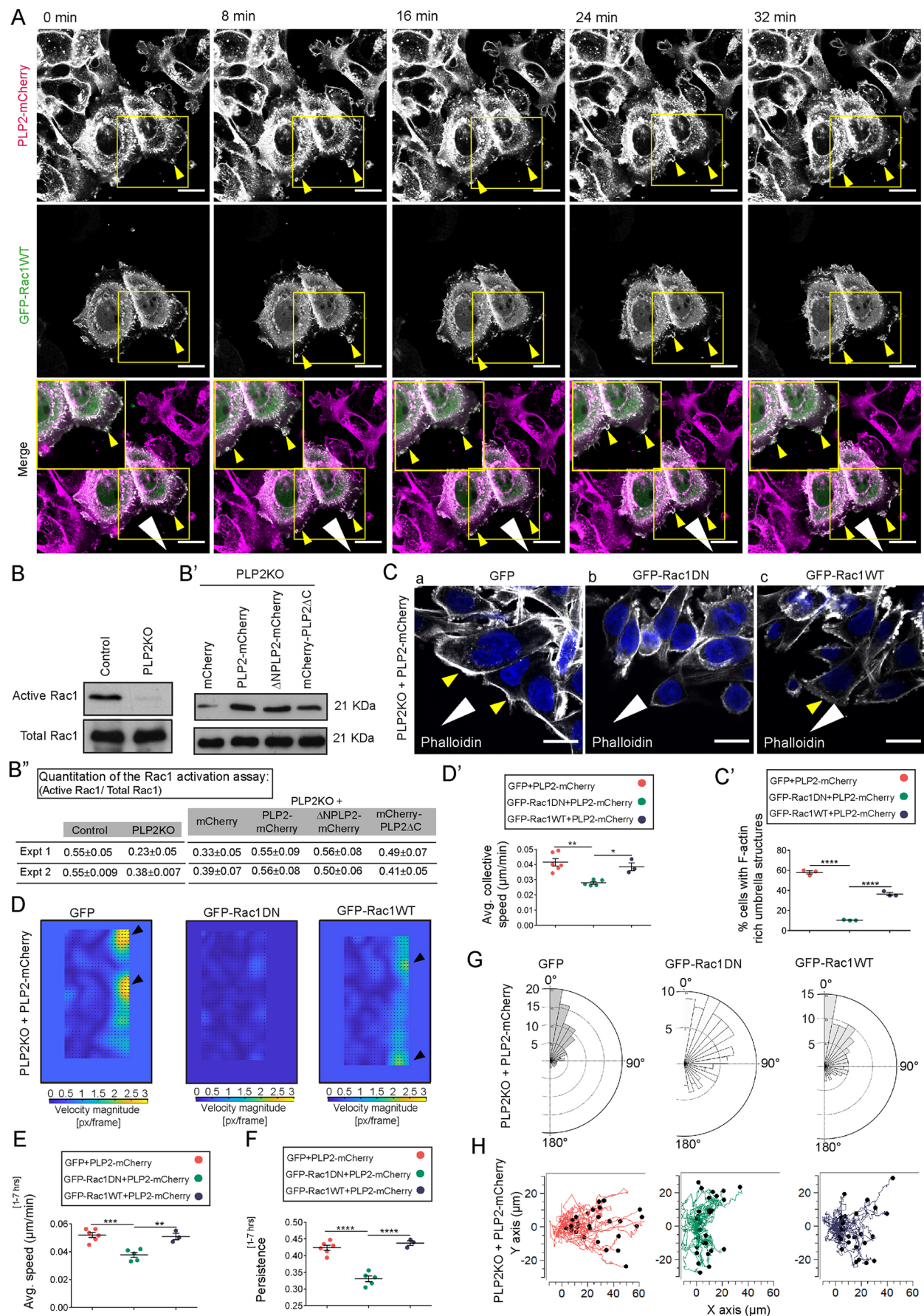
Fig. 6. See next page for legend.

Fig. 6. Rac1 activation contributes to PLP2-mediated CCM. (A) PLP2-mCherry colocalizes with GFP-Rac1WT at the leading edge during CCM (4 h post-wound). (B–B″) Rac1 activation assay (experiment 1). (B,B′) Control and PLP2KO (B) and PLP2KO cells overexpressing mCherry, PLP2-mCherry, ΔNPLP2-mCherry or mCherry-PLP2ΔC (B′) were grown to confluence and scratch wounded. Cells were harvested at 4 h post-wound and lysed in 50 mM Tris-HCl (pH 7.2), 1% Triton X-100, 500 mM NaCl, 10 mM MgCl$_2$, 1 mM PMSF and protease inhibitor cocktail. Cleared lysates were incubated with GST-PAK PBD bound to glutathione-coupled agarose beads for 1 h. Beads were washed three times in 50 mM Tris-HCl (pH 7.2), 150 mM NaCl, 10 mM MgCl$_2$. The bound proteins were eluted from beads by addition of SDS sample loading buffer, resolved by 12% SDS-PAGE and immunoblotted using anti-Rac1 antibody to capture active Rac1 population (upper lanes). The total amount of Rac1 in the whole-cell lysates (10% of total lysates used for activation assay) was determined by western blotting (lower lanes). (B″) Quantitation for experiments 1 and 2 of Rac1 activation assay represented as the ratio of active Rac1 to total Rac1. Representative blots for experiment 2 are shown in Fig. S6B″. (C–H) Wound scratch assay performed on PLP2KO cells co-expressing PLP2-mCherry and GFP, GFP-Rac1DN or GFP-Rac1WT. (C) F-actin-rich umbrella-like structures at the leading edge as observed during 4 h post-wound. (C′) Quantification of the number of cells from the first row, containing F-actin-rich lamellipodia (umbrella)-like structures. Data are presented as mean±s.e.m. for framewise percentage of PLP2KO cells co-expressing PLP2-mCherry and GFP [*n*=433 (134+155+144)], GFP-Rac1DN [*n*=905 (314+330+261)] or GFP-Rac1WT [*n*=405 (133+145+127)] from three independent experiments (*N*=3). (D,D′) PIV analysis, (D) velocity heatmaps (1 pixel=0.586 μm; one frame=15 min; high-speed zones, yellow regions pointed at by black arrowheads) and (D′) average collective speed measured between 1 h and 7 h post-wound from six, five and three independent experiments for PLP2KO cells co-expressing PLP2-mCherry and GFP, GFP-Rac1DN or GFP-Rac1WT, respectively. (E–H) Track analysis. (E) Average speed and (F) persistence measured between 1 h and 7 h post-wound for PLP2KO cells co-expressing PLP2-mCherry and GFP (*n*=414), GFP-Rac1DN (*n*=315) or GFP-Rac1WT (*n*=267) from six, five and three independent experiments, respectively. (G) Rose plots of angle trajectories. The magnitude of each bar indicates a fraction of cells with the indicated angle trajectory. Data are presented for PLP2KO cells co-expressing PLP2-mCherry and GFP (*n*=323), GFP-Rac1DN (*n*=386) or GFP-Rac1WT (*n*=386) from five, six and three independent experiments, respectively. (H) Trajectories of 30 representative cells or tracks measured over 12 h. For C′, D′–F, data are presented as scatter plots with mean±s.e.m.; *n*=number of cells or tracks. Statistical significance was calculated using one-way ANOVA; *P<0.05, **P<0.005, ***P<0.0005, ****P<0.0001. White arrowheads indicate the direction of migration; yellow arrowheads indicate (A) co-dynamics of PLP2-mCherry and GFP-Rac1WT, and (C) localization of F-actin at the migrating edges. Scale bars: 15 μm; insets are zoomed images of the yellow outlined regions.

et al., 2013; You et al., 2015) and Wnt protein (Hu et al., 2019). Our findings on exosomal PLP2 driving CCM in colon cancer epithelium is a novel addition to the list. This information will open up new windows for studying the mechanistic details of exosomal PLP2-mediated CCM, revealing the pathophysiological relevance of PLP2 in colon cancer progression.

Taken together, the results from the current study have unraveled the role of PLP2 in the CCM of colon cancer epithelium and thereby improved the current understanding of CRC progression via CCM.

MATERIALS AND METHODS
Cell lines and cell culture conditions
SW480 (CCL-228) and Caco-2 (HTB-37) cell lines were purchased from the cell repository of National Centre for Cell Science (NCCS) (https://www.nccs.res.in/index.php/TeamsNCCS/Repositories) (McGarrity, 1979) and authenticated for contamination. SW480 cells were maintained in Dulbecco's modified Eagle medium (DMEM) with 10% fetal bovine serum (FBS), 100 μg/ml penicillin, 100 μg/ml streptomycin at 37°C with 5% CO$_2$. Caco-2 cells were grown in Eagle minimum essential medium (EMEM) (minimum essential medium supplemented with 0.11 mg/ml sodium pyruvate and non-essential amino acid) with 20% FBS and 100 μg/ml penicillin–streptomycin at 37°C with 5% CO$_2$.

The SW480 stable cell line was grown in DMEM with 10% FBS, 100 μg/ml penicillin–streptomycin, and 500 μg/ml G418 at 37°C with 5% CO$_2$. For transient transfection, cells were grown in four-well plates or on coverslips in 24-well plates 36 h before transfection. At 60–80% cell confluence, cells were transfected with 0.5 μg plasmid DNA using Lipofectamine 2000 transfection reagent.

Antibodies, constructs and reagents
The following primary antibodies were used (IF, immunofluorescence; WB, western blotting): mouse monoclonal antibodies against GM130 (BD Transduction Laboratories 610822; WB, 1:1000), vinculin (Sigma-Aldrich V9131; WB, 1:1000, IF, 1:400), Alix (also known as PDCD6IP; Santa Cruz Biotechnology sc-53538; WB, 1:1000), nucleoporin (Santa Cruz Biotechnology sc-48373; WB, 1:500), Tsg101 (AbD Serotec, Bio-Rad MCA3515Z; WB, 1:500), GFP (Roche 11814460001; WB, 1:2000), CD63 (DSHB H5C6; IF, 1:500), tubulin (Sigma-Aldrich T6557; WB, 1:3000), cortactin (Millipore 05-180; IF, 1:300), Rac1 (BD Transduction Laboratories 610651; WB, 1:1000), Rab27a (Abcam ab55667; IF, 1:10); rabbit monoclonal antibodies against ZO-1 [Cell Signaling Technology (D7D12) 8193; WB, 1:1000, IF, 1:250], occludin (Abcam ab216327; WB, 1:1000, IF, 1:200), PLP2 (Abcam ab180131; WB, 1:3000, IF, 1:250); rabbit polyclonal antibody against actin (Sigma-Aldrich A2066; WB, 1:3000); and rat monoclonal antibody against mCherry (Invitrogen M11217; WB, 1:1000). The anti-Rac1 antibody was a gift from Prof. Alexis Gautreau (Ecole Polytechnique, Paris, France).

Primary antibodies were detected with Alexa Fluor 488-, 568- or 647-conjugated (Invitrogen Molecular Probes; IF, 1:500) or horseradish peroxidase (HRP)-conjugated (WB, 1:20,000) goat anti-mouse, anti-rabbit or anti-rat IgG. Alexa Fluor 568- or 647-conjugated phalloidin (Thermo Fisher Scientific A12379 and A12380, respectively; IF, 1:100) was used to detect the actin cytoskeleton.

The PLP2-GFP construct was obtained by cloning the full-length *PLP2* gene into the pEGFP-N1 vector (Addgene). Similarly, PLP2-mCherry and ΔNPLP2-mCherry were obtained by cloning the full-length *PLP2* and *ΔNPLP2* gene, respectively, into the pmCherry-N1 vector (Addgene). mCherry-PLP2ΔC was obtained by cloning the *PLP2ΔC* gene into the pmCherry-C1 vector (Addgene). Cortactin-pmCherryC1 (Addgene #27676), pGEX6P1-mCherry-Nanobody (Addgene #70696) and pGEX6P1-GFP-Nanobody (Addgene #61838) were purchased from Addgene. The GBP clone was further subcloned into a pGEX-6P1 vector for improved expression of GST-tagged GBP. The GST-PBD construct was a gift from Prof. Richard Cerione (Cornell University, Ithaca, NY, USA). pCDNA3Rac1eGFPWT and cB6GFPRac1N17 (GFPRac1DN) were gifts from Prof. Marino Zerial (Max Planck Institute of Molecular Cell Biology and Genetics, Dresden, Germany). mEmerald ZO-1-C14 (Addgene #54316) was a gift from Dr Tamal Das (Tata Institute of Fundamental Research, Hyderabad, India).

The following reagents were used in different experiments: NSMase2 inhibitor GW4869 (Sigma-Aldrich D1692), Mitomycin C (Sigma-Aldrich M4287), Geneticin or G418-sulphate (Gibco 11811-031), sodium pyruvate (Sigma-Aldrich P2256), non-essential amino acid (Gibco 11140-050), MTT or Thiazolyl Blue Tetrazolium Bromide (Sigma-Aldrich M2128), Lipofectamine 2000 (Thermo Fisher Scientific 11668-027), Lipofectamine Cas9 plus (Invitrogen A36496) and Lipofectamine CRISPRMAX (Invitrogen CMAX00003), fluorescein isothiocyanate (FITC)-dextran (Thermo Fisher Scientific D1823), SYBR® Green PCR Master Mix (Applied Biosystems 4367659), High-Capacity cDNA Reverse Transcription Kit (Applied Biosystems 4368814), Accuprime *Pfx* DNA Polymerase (Thermo Fisher Scientific 12344-024), 10× Accuprime *Pfx* Reaction Mix (Thermo Fisher Scientific P/N55013), CloneJET PCR Cloning Kit (Thermo Fisher Scientific K1232), specific restriction enzymes (New England Biolabs), T4 DNA ligase (New England Biolabs M0202S), Miniprep Kit (Qiagen 27106), RNA extraction kit (Invitrogen 12183018A), Gel Extraction Kit (GSure G4629A), ECL Western Blotting Detection Reagent (Bio-Rad 1705060).

Generation of stable cell lines
To generate a stable cell line, 2×10^5 cells were seeded in a four-well plate and transfected with PLP2-GFP or PLP2-mCherry using Lipofectamine
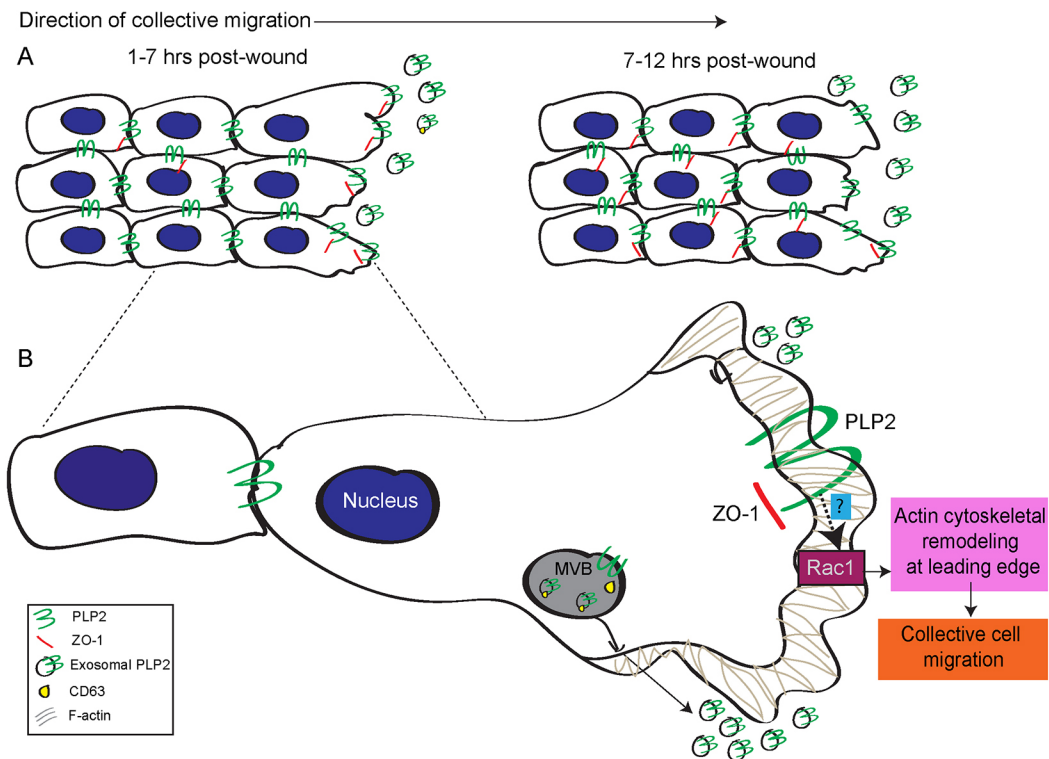
Fig. 7. Proposed model for PLP2–ZO-1-mediated CCM. (A) Moving cell collectives, showing maximum dynamics for velocity and directionality during 1–7 h post-wound (peak CCM hours), when PLP2–ZO-1 association is localized mostly to the lamellipodia like umbrella-shaped protrusions at the leading edge of the cells. Post-7 h, ZO-1 shows more pronounced localization at the CCJs. (B) During peak CCM hours, PLP2–ZO-1 association induces cytoskeletal remodeling at the leading edge, which involves Rac1 activation. The exosomal pool of PLP2 contributes to CCM synergistically with the endogenous pool of PLP2. Dotted line arrow with question mark (?) indicates involvement of additional molecular players bridging PLP2–ZO-1 association with Rac1 activation.

2000 after 36 h. Sixteen hours after transfection, the antibiotic selection was proceeded by adding G418 to the transfected cells at a concentration of 800 µg/ml in DMEM supplemented with 10% FBS and 100 µg/ml penicillin–streptomycin. The medium was changed every 72 h because the antibiotic degrades at 37°C. Cells that survived antibiotic stress proliferated and formed colonies. Several such clones were selected and grown separately. Each clone was detected for GFP expression by monitoring fluorescence through a Zeiss AX10 epifluorescence microscope. Clones with high GFP expression were further selected and grown in 150 mm dishes, and cryostocks were stored until further use.

siRNA transfection
Cells were seeded 36 h before performing siRNA transfection. A standard protocol, available at Horizon Discovery (https://horizondiscovery.com/en/gene-modulation/knockdown/sirna/on-targetplus-sirna), was used for transfection using Dharmafect as the transfection reagent. ON-TARGETplus SMARTpool siRNAs targeting PLP2 were purchased from Dharmacon and used at the working concentration of 20 nM. SW480 cells were transfected with SMARTpool siRNA against Scrambled (Scr; or non-targeting siRNA) or *PLP2*. The sequences of SMARTpool siRNAs are Scrambled #1, 5′-CGAACGGCCUGUACGAUGA-3′; Scrambled #2, 5′-GGCCAGACGCCCAACCAUA-3′; Scrambled #3, 5′-GCGAGCAGCCA-CCAAAUUG-3′; Scrambled #4, 5′-GGGAGUACCUGGCGUUUCC-3′; *PLP2* #1, 5′-GUACUGGGCCUAAUCGCUA-3′; *PLP2* #2, 5′-CAAA-UAAUCUCCUCGGUGU-3′; *PLP2* #3, 5′-GUUCGGCAGCCAAGA-CAUA-3′; and *PLP2* #4, 5′-AGAUGAUCCUUGCUGCUAU-3′. Transfected cells were used for further experiments, 72 h post transfection.

CRISPR-mediated PLP2KO cell line generation
Generation of the PLP2 knockout cell line was performed by CRISPR/Cas9 using an online CRISPR design tool (https://www.thermofisher.com/in/en/home/life-science/genome-editing/geneart-crispr/crispr-libraries/trueguide-grnas.html) from Thermo Fisher Scientific. A 20-nucleotide guide sequence was designed against human PLP2 isoform1. The targeted DNA sequence was GGATTGCCGCTATGAGGGTT in exon3 with protospacer adjacent motif sequence CGG. A negative control, non-targeting sgRNA (5′-AAAUGUGAGAUCAGAGUAAU-3′), which does not recognize any specific sequence was also used. One thousand cells were seeded per well of a 96-well plate 36 h before transfection. Cells were transfected with Cas9-sgRNA complex at a ratio of 250 ng/1.5 pmol per protein using Lipofectamine Cas9 plus and Lipofectamine CRISPRMAX reagents. Forty-eight hours after transfection, cells were serially diluted to achieve single-cell-derived colonies that were grown until 80% confluence. CRISPR knockout was confirmed by western blotting.

MTT assay
MTT assay was performed as described previously (Zhou et al., 2015) with minor modifications. Briefly, 10,000 cells per well of a 96-well plate were seeded and incubated at 37°C under 5% CO_2. Time 0 h was taken at an instance when cells got adhered, and consecutive time points of 24, 48, 72 and 96 h were calculated accordingly. At each time point, the MTT solution was added to each well containing complete medium to a final concentration of 0.5 mg/ml and incubated for 2 h at 37°C. After 2 h of incubation, cells were lysed using dimethyl sulfoxide (DMSO) and homogenized, and absorbance was measured at 550 nm.

Paracellular flux assay
Paracellular flux was measured as per the reported method (Balda et al., 1996) with minor modifications. Briefly, cells were grown on 0.8 µm filter placed in 24-well plates for 1 week. FITC-dextran of 70 kDa was dissolved in P buffer (10 mM Hepes pH 7.4, 1 mM sodium pyruvate, 10 mM glucose, 3 mM $CaCl_2$, 145 mM NaCl) to prepare a stock of 10 mg/ml and diluted to

1 mg/ml with P buffer. On the assay day, 200 µl P buffer was added to the basal side of the cells, and 50 µl of the tracer solution was added to the apical side of the cells, which were incubated at 37°C for 3 h. The P buffer containing tracer solution was then collected from the basal side of the cells, and FITC-dextran fluorescence was measured with a fluorometer (excitation, 492 nm; emission, 520 nm).

PSIPRED prediction analysis
Secondary structure prediction was performed using the PSIPRED online tool (http://bioinf.cs.ucl.ac.uk/psipred/).

Exosome isolation and purification
Exosome isolation from cell culture supernatants was performed as described previously (Ji et al., 2013) with minor modifications. Briefly, cells were treated with serum-free medium (conditioned medium) for 48 h, and the conditioned medium was collected and centrifuged at 300 g for 5 min, followed by 2000 g for 25 min, to remove floating cells and cell debris, respectively. For exosome isolation, the supernatant obtained after 2000 g centrifugation was further centrifuged at 10,000 g for 30 min at 4°C to pellet small microvesicles. Crude exosomes were precipitated by ultracentrifugation of the supernatant at 100,000 g for 18 h at 4°C. The crude exosome pellet was then purified using Histodenz (Sigma-Aldrich) density gradient. Briefly, a discontinuous Histodenz gradient was prepared by diluting a stock solution of 60% w/v Histodenz solution with 0.25 M sucrose/10 mM Tris-HCl pH 7.5 to generate 40% w/v, 20% w/v, 10% w/v and 5% w/v Histodenz solutions from bottom to top. The crude exosomes were resuspended in PBS and loaded onto the top of the gradient. The gradient was then centrifuged at 100,000 g for 18 h at 4°C. Four individual fractions were collected (starting from the top of the gradient with increasing density), and each fraction was diluted with a 4× volume of PBS. After centrifugation at 100,000 g for 3 h at 4°C, the supernatants were discarded, and pellets were washed with 1 ml PBS. The pellet was then either resuspended for NTA/treatment or lysed for protein extraction. The exosomes obtained from PLP2-GFP cells were named as 'exosome$^{PLP2-GFP}$'.

For GW4869 treatment (Guo et al., 2015), 50% confluent cells were treated with serum-free medium containing 5 µM GW4869 (dissolved in DMSO) in which the cells were incubated for 48 h at 37°C. Culture supernatants were then collected for exosome isolation and purification.

Treatment of cells with purified exosomes was performed as described previously (Hoshino et al., 2013) with minor modifications. First, 80% confluent PLP2KO cells were treated with 8×10^6 exosome$^{PLP2-GFP}$ (as per NTA quantification) in serum-free medium for 5 h. Cells were then washed with PBS and incubated at 37°C for 5 h and 16 h, respectively. Post-incubated cells were then washed and used for further experiments.

NTA
NTA was carried out using a Nanosight NS300 system (Malvern Panalytical, Malvern, UK) (Filipe et al., 2010), with exosomes resuspended in PBS and further diluted 100–200 times during analysis. The results are presented as the mean±s.e.m. of three independent experiments.

TEM for characterizing purified exosomes:
Aliquots (10 µl) of density gradient-purified exosomes were fixed with 10 µl of 2% (v/v) electron microscopy-grade glutaraldehyde and incubated for 30 min at room temperature. A 6 µl aliquot of fixed exosome solution was then absorbed onto 400-mesh carbon-coated copper grids (Ted Pella). Excess material was removed by blotting, and samples were air dried and viewed using a TALOS 200 kV S-FEG (FEI) transmission electron microscope as previously described (Guo et al., 2015).

RNA extraction and quantitative RT-PCR
Total RNA was isolated from the cells using an RNA isolation kit (Invitrogen) according to the manufacturer's protocol. cDNA was prepared using the High-Capacity cDNA Reverse Transcription Kit (Applied Biosystems). Real-time quantitative PCR reactions were performed using the SYBR® Green PCR Master Mix (Applied Biosystems) and corresponding primers on an Applied Biosystems 7300 Real-Time PCR System. *GAPDH* was used as an internal control to check the efficiency of cDNA synthesis and PCR amplification.

Protein extraction and immunoblotting
Cells were harvested and lysed in lysis buffer (50 mM Tris-HCl pH 7.4, 150 mM NaCl, 1 mM EDTA and 1% Triton X-100) supplemented with 10 µg/ml protease inhibitor cocktail (PIC). Cell debris was removed by centrifuging at 15,000 g for 15 min at 4°C. Protein concentration was estimated using a Micro BCA Protein Assay Kit (Thermo Fisher Scientific). Samples were prepared by adding 1× SDS loading dye and separated by SDS-PAGE, followed by transfer to a nitrocellulose membrane (0.45 µm; GE Healthcare 10600002). The membrane was blocked with 5% skim milk (SM Powder, HIMEDIA; GRM1254) for 1 h and then incubated for 2 h at room temperature with the respective primary antibodies. To detect the bound antibody signal, the membrane was incubated with HRP-conjugated secondary antibody, and protein bands were detected using chemiluminescence-based ECL Western Blotting Detection Reagent.

GST-CBP or GST-GBP expression, purification and respective TRAP pull-down assays
Clone for GBP was purchased from Addgene and subcloned into pGEX-6P1 vector for improved expression of GST-tagged GBP. pGEX6P1-mCherry-Nanobody construct from Addgene was directly used to express GST-CBP. GST-tagged GBP or CBP was expressed in BL21-DE3 cells that were lysed in lysis buffer containing PBS pH 7.4, 1 mM DTT, 1 mM EDTA, 1% Triton X-100, 200 µM PMSF and 10 µg/ml PIC and centrifuged at 19,000 g for 30 min at 4°C to remove cell debris. The supernatant was collected and used for purification of GST-CBP or GST-GBP through its binding onto the glutathione agarose beads (Pierce, Thermo Fisher Scientific) and eluted with 50 mM Tris-HCl pH 8.0, 120 mM NaCl and 20 mM reduced glutathione, concentrated, aliquoted and stored until use.

The recombinant protein was quantified prior to Cherry or GFP-trap pull-down assays. For each reaction, 30 µg GST-tagged bait was added to the glutathione agarose beads and incubated for 1 h at 4°C on the rotamer. Unbound bait was removed by washing beads three times with 1× PBS while spinning at 4°C and 500 g for 5 min. Meanwhile, to prepare lysate, mCherry vector or mCherry fusion proteins were overexpressed in six-well format in the respective cells. Sixteen hours after transfection, cells were lysed in 50 mM Tris-HCl pH 7.4, 150 mM NaCl, 1 mM EDTA and 1% Triton X-100 with 10 µg/ml PIC and cleared by centrifugation at 19,000 g at 4°C for 15 min. Cleared lysates were mixed with 30 µg GST-CBP or GST-GBP bound to the glutathione agarose beads and incubated for 2 h. The beads bound with GBP-GFP or CBP-mCherry protein complexes were then washed three times with PBS, followed by elution using a 2× SDS sample loading buffer. Samples were then separated on 8% SDS gel followed by immunoblotting, and 10% of the whole-cell lysates was used as inputs.

Rac1 activation assay
GST-PBD was purified as reported earlier (Phillips et al., 2008). Rac1 activation assay was performed as reported earlier (Meriane et al., 2002; Plutoni et al., 2016) with minor modifications. Briefly, control, PLP2KO and PLP2KO cells overexpressing mCherry, PLP2-mCherry, ΔNPLP2-mCherry or mCherry-PLP2ΔC were grown to confluence and scratch wounded. Cells were harvested at 4 h post-wound and lysed in 50 mM Tris-HCl pH 7.2, 1% Triton-X-100, 500 mM NaCl, 10 mM MgCl₂, 1 mM PMSF and protease inhibitor cocktail. Cleared lysates were incubated with GST-PBD bound to glutathione-coupled agarose beads for 1 h. Beads were washed three times in 50 mM Tris-HCl pH 7.2, 150 mM NaCl, 10 mM MgCl₂. The bound proteins were eluted from beads by addition of SDS sample loading buffer, resolved by 12% SDS-PAGE and immunoblotted using anti-Rac1 antibody to capture the active Rac1 population. The total amount of Rac1 in the whole-cell lysates (10% of total lysates used for activation assay) was also determined by western blotting.

Immunocytochemistry

Cells were fixed in 4% paraformaldehyde for 15 min at room temperature. Alternatively, cells were fixed in 100% prechilled methanol for 15 min at −20°C. Immunofluorescence staining was performed on fixed cells permeabilized with 0.1% Triton X-100 for 10 min at room temperature, followed by blocking with 5% FBS in PBS before staining with respective antibodies. The coverslips were mounted using Mowiol (Calbiochem 475904) on glass slides and imaged using a Zeiss LSM 780 laser-scanning confocal microscope with the Zen 2010 software.

Confocal image analysis

Confocal images were analyzed mainly using ImageJ software. Colocalization analysis was performed using the ImageJ 'colocalization threshold' plugin (Ross, 2007). Regions of interest (ROIs) were created as per requirement, and the selected ROI was applied for image processing and measuring Pearson's correlation coefficients. Data from three independent experiments were exported to GraphPad Prism 6 software and tabulated accordingly. The intensity plots of the fluorescent intensity (y-axis) against distance (x-axis) represent the overlap between channels in individual cases.

For object-based colocalization analysis, data from three independent experiments were subjected to analysis by the automated image analysis program Motion Tracking (http://motiontracking.mpi-cbg.de). The cells were randomly selected for imaging in a given experimental setup and chosen for quantification thereof. At a minimum, 400 cells were used for quantification from three independent experiments. The objects were identified as vesicles in each channel based on their size, fluorescence intensity and image background by Motion Tracking software (Collinet et al., 2010; Rink et al., 2005). Objects detected in two different channels were considered to be colocalized if the relative overlap of respective areas was >35%. The apparent colocalization value was calculated as the ratio of integral intensities of colocalized objects to the integral intensities of all objects carrying a given marker and varied from 0.0 to 1.0. The colocalization-by-chance (random colocalization) was estimated by random permutation of objects localization in different channels. The apparent colocalization was corrected for random colocalization. The obtained colocalization value was converted into the percentage values by multiplying by 100, and this represents the percentage population of the candidate protein (PLP2 or PLP2-GFP) that colocalizes with an endosomal marker.

Confocal live-cell microscopy

Stable cells or cells transfected with respective constructs were seeded on glass-bottom dishes. Cells in respective complete medium were incubated further in culture condition while imaging with an Olympus FV3000 confocal laser-scanning microscope with a 60× Plan Apo N objective (oil, 1.42 NA) on an inverted stage. Images were acquired and processed using FV31S-SW software and ImageJ software, respectively.

Wound scratch assay, live-cell video microscopy and time-lapse imaging

Cells ($3×10^5$) were plated in four-well dishes for 48 h to achieve the desired cell confluence. Cells were treated with Mitomycin C (10 μg/ml) (Glenn et al., 2016) for 4 h before creating the wound using a 10 μl tip to allow the cells to migrate into the cell-free areas. Live-cell video microscopy was conducted using a JuLI™Br inverted microscope (NanoEnTek) equipped with a station unit that runs inside a CO_2-regulated incubator and a scope unit that runs outside the incubator. Phase-contrast images were captured every 15 min overnight using a 4× objective and a CMOS camera with a pixel length of 0.586 μm.

Individual cell tracking and measurements of cell speed, persistence and angular distribution of the tracks

The TrackMate (v3.8.0) plugin (Tinevez et al., 2017) of ImageJ (version 1.52p) software was used to track individual cells from the first three layers of cells facing the wound. The following parameters were assigned while computing the tracks using TrackMate: detector, LoG; blob diameter, 15 pixels; threshold, 0.8–1; simple LAP tracker; linking maximum distance, 20–25 pixel; gap closing maximum distance, 12 pixels; gap closing maximum frame gap, 1; filter on track, track duration >47.75 (for analyzing 1 to 48 frames). The spatiotemporal information (X and Y position in each frame) of the tracks was used to compute average speed (v), persistence and track angles using a program coded in Fortran 77. Persistence is measured as the ratio of net displacement and total migration distance of individual cells. The values of these parameters were further verified using the chemotaxis and migration tool (version 2.0) available on www.ibidi.com. The tracks were plotted using the same tool for presentation. Track angle distributions were generated using the program Rose.Net (version 0.10.0.0), as described previously (Plutoni et al., 2016).

PIV

PIV analysis, a whole-field cross-correlation technique that provides local displacements in real time for the entire cell monolayer, was carried out using the PIVlab tool (version 2.31) (Thielicke and Stamhuis, 2014) in MATLAB (version 2.98) (MathWorks). We used a particle count-based window size, as suggested by the tool, with subsequent two more passes with the final interrogation window size of 75×75 pixels and a 50% overlap. The analysis was carried out in a window with a dimension of 800×1560 pixels. The velocity vector field was further smoothened by 'Smoothn' (Garcia, 2011). Speed, horizontal velocity component (u) and angles were extracted from the PIV results and further used to generate a kymograph to study the dynamics of the process. Local order parameter (Petitjean et al., 2010; Zhang et al., 2017a) was calculated for the vectors by computing cosine of the respective angles [Cos(θ)]. The value of this parameter ranges between −1 and +1, where +1 represents collective movement perpendicular to the wound border or towards +X (refer to Fig. 2B), and −1 represents a collective movement towards −X (Petitjean et al., 2010; Zhang et al., 2017a).

To understand the time dependence of these parameters, we chose a section, X, from the active zone and plotted u or s against time at X. To understand the time dependence of these parameters, we chose a section, X, from the active zone and plotted u or s against time at X. Kymographs of horizontal velocity component (u) and s were computed by plotting Y-averaged values of each parameter for different X values against time (where the x-axis is perpendicular to the wound border, and Y represents parallel to the wound border; refer to Fig. 2B). Heatmaps were generated in GNUPLOT (version 5.1; http://www.gnuplot.info) (1 pixel=0.586 μm; one frame=15 min).

Statistical analysis

For the statistical evaluation of the datasets from quantitative image analysis, paired or unpaired two-tailed Student's t-test or one-way ANOVA was performed using GraphPad Prism6 software version 6.01. Datasets are presented as means±s.e.m. for each independent experiment, and $P<0.05$ was considered statistically significant. Data were assumed to be distributed normally, but this was not otherwise tested. The number of samples, images and experiments used for quantification are mentioned in the respective figure legends. In all figures, n=number of cells or tracks and N=number of experiments.

References

Andreu, Z. and María, Y.-M. (2014). Tetraspanins in extracellular vesicle formation and function. *Front. Immunol.* **5**, 1-12. doi:10.3389/fimmu.2014.00442

Aznavoorian, S., Liotta, L. A. and Kupchik, H. Z. (1990). Characteristics of invasive and noninvasive human colorectal adenocarcinoma cells. *J. Natl. Cancer Inst.* **82**, 1485-1492. doi:10.1093/jnci/82.18.1485

Balda, M. S., Whitney, J. A., Flores, C., González, S., Cereijido, M. and Matter, K. (1996). Functional dissociation of paracellular permeability and transepithelial electrical resistance and disruption of the apical-basolateral intramembrane diffusion barrier by expression of a mutant tight junction membrane protein. *J. Cell Biol.* **134**, 1031-1049. doi:10.1083/jcb.134.4.1031

Becker, A., Thakur, B. K., Weiss, J. M., Kim, H. S., Peinado, H. and Lyden, D. (2016). Extracellular vesicles in cancer: cell-to-cell mediators of metastasis. *Cancer Cell* **30**, 836-848. doi:10.1016/j.ccell.2016.10.009

Berger, D., Park, D. O. Y., Iafrate, A. J., Zukerberg, L. R. and Chung, D. C. (2010). Epithelial to mesenchymal transition is impaired in colon cancer cells with microsatellite instability. *YGAST* **138**, 1406-1417.

Bobrie, A., Colombo, M., Raposo, G. and Théry, C. (2011). Exosome secretion: molecular mechanisms and roles in immune responses. *Traffic* **12**, 1659-1668. doi:10.1111/j.1600-0854.2011.01225.x

Bozzuto, G., Condello, M. and Molinari, A. (2015). Migratory behaviour of tumour cells: a scanning electron microscopy study. *Ann. Ist. Super. Sanita* **51**, 139-147.

Breitwieser, G. E., McLenithan, J. C., Cortese, J. F., Shields, J. M., Oliva, M. M., Majewski, J. L., Machamer, C. E. and Yang, V. W. (1997). Colonic epithelium-enriched protein A4 is a proteolipid that exhibits ion channel characteristics. *Am. J. Physiol. Physiol.* **272**, C957-C965. doi:10.1152/ajpcell.1997.272.3.C957

Chen, Y., Hueng, D. and Tsai, W. (2018). Proteolipid protein 2 overexpression indicates aggressive tumor behavior and adverse prognosis in human gliomas.

Cheung, K. J. and Ewald, A. J. (2016). A collective route to metastasis: seeding by tumor cell clusters. *Science (80-.).* **352**, 167-169. doi:10.1126/science.aaf6546

Collinet, C., Stöter, M., Bradshaw, C. R., Samusik, N., Rink, J. C., Kenski, D., Habermann, B., Buchholz, F., Henschel, R., Mueller, M. S. et al. (2010). Systems survey of endocytosis by multiparametric image analysis. *Nature* **464**, 243-249. doi:10.1038/nature08779

Colombo, M., Raposo, G. and Théry, C. (2014). Biogenesis, secretion, and intercellular interactions of exosomes and other extracellular vesicles. *Annu. Rev. Cell Dev. Biol.* **30**, 255-289. doi:10.1146/annurev-cellbio-101512-122326

Das, T., Safferling, K., Rausch, S., Grabe, N., Boehm, H. and Spatz, J. P. (2015). A molecular mechanotransduction pathway regulates collective migration of epithelial cells. *Nat. Cell Biol.* **17**, 276-287. doi:10.1038/ncb3115

Ebnet, K., Schulz, C. U., Meyer Zu Brickwedde, M.-K., Pendl, G. G. and Vestweber, D. (2000). Junctional adhesion molecule interacts with the PDZ domain-containing proteins AF-6 and ZO-1. *J. Biol. Chem.* **275**, 27979-27988. doi:10.1074/jbc.M002363200

Fanning, A. S., Jameson, B. J., Jesaitis, L. A. and Anderson, J. M. (1998). The tight junction protein ZO-1 establishes a link between the transmembrane protein occludin and the actin cytoskeleton. *J. Biol. Chem.* **273**, 29745-29753. doi:10.1074/jbc.273.45.29745

Feng, Z., Zhou, W., Wang, J., Qi, Q., Han, M., Kong, Y., Hu, Y., Zhang, Y., Chen, A., Huang, B. et al. (2020). Reduced expression of proteolipid protein 2 increases ER stress-induced apoptosis and autophagy in glioblastoma. *J. Cell. Mol. Med.* **24**, 2847-2856. doi:10.1111/jcmm.14840

Filipe, V., Hawe, A. and Jiskoot, W. (2010). Critical evaluation of nanoparticle tracking analysis (NTA) by NanoSight for the measurement of nanoparticles and protein aggregates. *Pharm. Res.* **27**, 796-810. doi:10.1007/s11095-010-0073-2

Foster, R., Hu, K. Q., Lu, Y., Nolan, K. M., Thissen, J. and Settleman, J. (1996). Identification of a novel human Rho protein with unusual properties: GTPase deficiency and in vivo farnesylation. *Mol. Cell. Biol.* **16**, 2689-2699. doi:10.1128/MCB.16.6.2689

Friedl, P. and Gilmour, D. (2009). Collective cell migration in morphogenesis, regeneration and cancer. *Nat. Rev. Mol. Cell Biol.* **10**, 445-457. doi:10.1038/nrm2720

Friedl, P. and Mayor, R. (2017). Tuning collective cell migration by cell–cell junction regulation. *Cold Spring Harb. Perspect. Biol.* **9**, a029199. doi:10.1101/cshperspect.a029199

Friedl, P., Zanker, K. S., Friedl, P., Noble, P. B., Zanker, K. S., Walton, P. A., Laird, D. W., Chauvin, P. J., Tabah, R. J. and Black, M. (1995). Migration of coordinated cell clusters in mesenchymal and epithelial cancer explants in vitro. *Cancer Res.* **55**, 4557-4560.

Friedl, P., Locker, J., Sahai, E. and Segall, J. E. (2012). Classifying collective cancer cell invasion. *Nat. Cell Biol.* **14**, 777-783. doi:10.1038/ncb2548

Furuse, M., Itoh, M., Hirase, T., Nagafuchi, A., Yonemura, S., Tsukita, S. and Tsukita, S. (1994). Direct association of occludin with ZO-1 and its possible involvement in the localization of occludin at tight junctions. *J. Cell Biol.* **127**, 1617-1626. doi:10.1083/jcb.127.6.1617

Garcia, D. (2011). A fast all-in-one method for automated post-processing of PIV data. *Exp. Fluids* **50**, 1247-1259. doi:10.1007/s00348-010-0985-y

Glenn, H. L., Messner, J. and Meldrum, D. R. (2016). A simple non-perturbing cell migration assay insensitive to proliferation effects. *Sci. Rep.* **6**, 31694. doi:10.1038/srep31694

González-Tarragó, V., Elosegui-Artola, A., Bazellières, E., Oria, R., Pérez-González, C. and Roca-Cusachs, P. (2017). Binding of ZO-1 to α5β1 integrins regulates the mechanical properties of α5β1-fibronectin links. *Mol. Biol. Cell* **28**, 1847-1852. doi:10.1091/mbc.e17-01-0006

Grada, A., Otero-Vinas, M., Prieto-Castrillo, F., Obagi, Z. and Falanga, V. (2017). Research techniques made simple: analysis of collective cell migration using the wound healing assay. *J. Invest. Dermatol.* **137**, e11-e16. doi:10.1016/j.jid.2016.11.020

Guo, B. B., Bellingham, S. A. and Hill, A. F. (2015). The neutral sphingomyelinase pathway regulates packaging of the prion protein into exosomes. *J. Biol. Chem.* **290**, 3455-3467. doi:10.1074/jbc.M114.605253

Haeger, A., Krause, M., Wolf, K. and Friedl, P. (2014). Cell jamming: collective invasion of mesenchymal tumor cells imposed by tissue confinement. *Biochim. Biophys. Acta Gen. Subj.* **1840**, 2386-2395. doi:10.1016/j.bbagen.2014.03.020

Haeger, A., Wolf, K., Zegers, M. M. and Friedl, P. (2015). Collective cell migration: guidance principles and hierarchies. *Trends Cell Biol.* **25**, 556-566. doi:10.1016/j.tcb.2015.06.003

Hashimoto, K. and Shimizu, M. (1993). Epithelial properties of human intestinal Caco-2 cells cultured in a serum-free medium. *Cytotechnology* **13**, 175-184. doi:10.1007/BF00749813

Hegerfeldt, Y., Tusch, M., Bröcker, E. B. and Friedl, P. (2002). Collective cell movement in primary melanoma explants: Plasticity of cell-cell interaction, β1-integrin function, and migration strategies. *Cancer Res.* **62**, 2125-2130.

Hoshino, D., Kirkbride, K. C., Costello, K., Clark, E. S., Sinha, S., Grega-Larson, N., Tyska, M. J. and Weaver, A. M. (2013). Exosome secretion is enhanced by invadopodia and drives invasive behavior. *Cell Rep.* **5**, 1159-1168. doi:10.1016/j.celrep.2013.10.050

Hu, Y.-B., Yan, C., Mu, L., Mi, Y. L., Zhao, H., Hu, H., Li, X.-L., Tao, D.-D., Wu, Y.-Q., Gong, J. P. et al. (2019). Exosomal Wnt-induced dedifferentiation of colorectal cancer cells contributes to chemotherapy resistance. *Oncogene* **38**, 1951-1965. doi:10.1038/s41388-018-0557-9

Hurwitz, S. N., Rider, M. A., Bundy, J. L., Liu, X., Singh, R. K. and Meckes, D. G. (2016). Proteomic profiling of NCI-60 extracellular vesicles uncovers common protein cargo and cancer type-specific biomarkers. *Oncotarget* **7**, 86999-87015. doi:10.18632/oncotarget.13569

Hurwitz, S. N., Nkosi, D., Conlon, M. M., York, S. B., Liu, X., Tremblay, D. C. and Meckes, D. G. (2017). CD63 regulates epstein-barr virus LMP1 exosomal packaging, enhancement of vesicle production, and noncanonical NF-κB signaling. *J. Virol.* **91**, 1-19. doi:10.1128/JVI.02251-16

Ilina, O. and Friedl, P. (2009). Mechanisms of collective cell migration at a glance. *J. Cell Sci.* **122**, 3203-3208. doi:10.1242/jcs.036525

Ilina, O., Bakker, G.-J., Vasaturo, A., Hoffman, R. M. and Friedl, P. (2011). Two-photon laser-generated microtracks in 3D collagen lattices: principles of MMP-dependent and -independent collective cancer cell invasion. *Phys. Biol.* **8**, 029501-029501. doi:10.1088/1478-3975/8/2/029501

Itoh, M., Furuse, M., Morita, K., Kubota, K., Saitou, M. and Tsukita, S. (1999). Direct binding of three tight junction-associated MAGUKs, ZO-1, ZO-2, and ZO-3, with the COOH Termini of Claudins. *J. Cell Biol.* **147**, 1351-1363. doi:10.1083/jcb.147.6.1351

Ji, H., Greening, D. W., Barnes, T. W., Lim, J. W., Tauro, B. J., Rai, A., Xu, R., Adda, C., Mathivanan, S., Zhao, W. et al. (2013). Proteome profiling of exosomes derived from human primary and metastatic colorectal cancer cells reveal differential expression of key metastatic factors and signal transduction components. *Proteomics* **13**, 1672-1686. doi:10.1002/pmic.201200562

Jolly, M. K., Boareto, M., Huang, B., Jia, D., Lu, M., Ben-Jacob, E., Onuchic, J. N. and Levine, H. (2015). Implications of the hybrid epithelial/mesenchymal phenotype in metastasis. *Front. Oncol.* **5**, 155. doi:10.3389/fonc.2015.00155

Karagiannis, G. S., Schaeffer, D. F., Cho, C.-K. J., Musrap, N., Saraon, P., Batruch, I., Grin, A., Mitrovic, B., Kirsch, R., Riddell, R. H. et al. (2014). Collective migration of cancer-associated fibroblasts is enhanced by overexpression of tight junction-associated proteins claudin-11 and occludin. *Mol. Oncol.* **8**, 178-195. doi:10.1016/j.molonc.2013.10.008

Kim, M. J., Cho, Y. B., Chun, H.-K., Lee, W. Y., Yun, S. H. and Kim, H. C. (2013). The expression of epithelial mesenchymal transition related factors in human colorectal cancer cell lines. *Korean J. Clin. Oncol.* **9**, 160-167. doi:10.14216/kjco. 13030

Ladoux, B. and Mège, R. M. (2017). Mechanobiology of collective cell behaviours. *Nat. Rev. Mol. Cell. Biol.* **18**, 743-757. doi:10.1038/nrm.2017.98

Lee, S. H. (2015). Intestinal permeability regulation by tight junction: implication on inflammatory bowel diseases. *Intest. Res.* **13**, 11. doi:10.5217/ir.2015.13.1.11

Leibovitz, A., Stinson, J. C., McCombs, W. B., III, McCoy, C. E., Mazur, K. C. and Mabry, N. D. (1976). Classification of human colorectal adenocarcinoma cell lines. *Cancer Res.* **36**, 4562-4569.

Loo, L.-H., Laksameethanasan, D. and Tung, Y.-L. (2014). Quantitative protein localization signatures reveal an association between spatial and functional divergences of proteins. *PLoS Comput. Biol.* **10**, e1003504. doi:10.1371/journal. pcbi.1003504

Maia, J., Caja, S., Strano Moraes, M. C., Couto, N. and Costa-Silva, B. (2018). Exosome-based cell-cell communication in the tumor microenvironment. *Front. Cell Dev. Biol.* **6**, 1-19. doi:10.3389/fcell.2018.00018

Matsuzawa, K., Himoto, T., Mochizuki, Y. and Ikenouchi, J. (2018). α-catenin controls the anisotropy of force distribution at cell-cell junctions during collective cell migration. *Cell Rep.* **23**, 3447-3456. doi:10.1016/j.celrep.2018.05.070

Mayor, R. and Etienne-Manneville, S. (2016). The front and rear of collective cell migration. *Nat. Rev. Mol. Cell Biol.* **17**, 97-109. doi:10.1038/nrm.2015.14

McGarrity, G. J. (1979). Sources of stable cell lines. *Methods Enzymol.* **58**, 439-444. doi:10.1016/S0076-6879(79)58158-0

McNeil, E., Capaldo, C. T. and Macara, I. G. (2006). Zonula occludens-1 function in the assembly of tight junctions in madin-darby canine kidney epithelial cells. *Mol. Biol. Cell* **17**, 1922-1932. doi:10.1091/mbc.e05-07-0650

Meriane, M., Charrasse, S., Comunale, F., Méry, A., Fort, P., Roux, P. and Gauthier-Rouvière, C. (2002). Participation of small GTPases Rac1 and Cdc42Hs in myoblast transformation. *Oncogene* **21**, 2901-2907. doi:10.1038/sj. onc.1205396

Mu, W., Rana, S. and Zöller, M. (2013). Host matrix modulation by tumor exosomes promotes motility and invasiveness. *Neoplasia (United States)* **15**, 875-887. doi:10.1593/neo.13786

Nieto, M. A., Huang, R. Y.-J., Jackson, R. A. and Thiery, J. P. (2016). EMT: 2016. *Cell* **166**, 21-45. doi:10.1016/j.cell.2016.06.028

Nobes, C. D., Lauritzen, I., Mattei, M.-G., Paris, S., Hall, A. and Chardin, P. (1998). A new member of the Rho family, Rnd1, promotes disassembly of actin filament structures and loss of cell adhesion. *J. Cell Biol.* **141**, 187-197. doi:10.1083/jcb.141.1.187

Oliva, M. M., Wu, T. C. and Yang, V. W. (1993). Isolation and characterization of a differentiation-dependent gene in the human colonic cell line HT29-18. *Arch. Biochem. Biophys.* **302**, 183-192. doi:10.1006/abbi.1993.1197

Ostrowski, M., Carmo, N. B., Krumeich, S., Fanget, I., Raposo, G., Savina, A., Moita, C. F., Schauer, K., Hume, A. N., Freitas, R. P. et al. (2010). Rab27a and Rab27b control different steps of the exosome secretion pathway. *Nat. Cell Biol.* **12**, 19-30. doi:10.1038/ncb2000

Ozawa, H., Sonoda, Y., Suzuki, T., Yoshida-hoshina, N., Funakoshi-Tago, M. and Kasahara, T. (2012). Knockdown of proteolipid protein 2 or focal adhesion kinase with an artificial microRNA reduces growth and metastasis of B16BL6 melanoma cells. *Oncol. Lett.* **3**, 19-24. doi:10.3892/ol.2011.422

Ozawa, M., Hiver, S., Yamamoto, T., Shibata, T., Upadhyayula, S., Mimori-Kiyosue, Y. and Takeichi, M. (2020). Adherens junction regulates cryptic lamellipodia formation for epithelial cell migration. *J. Cell Biol.* **219**, e202006196. doi:10.1083/jcb.202006196

Palmulli, R. and van Niel, G. (2018). To be or not to be… secreted as exosomes, a balance finely tuned by the mechanisms of biogenesis. *Essays Biochem.* **62**, 177-191. doi:10.1042/EBC20170076

Pankov, R., Endo, Y., Even-Ram, S., Araki, M., Clark, K., Cukierman, E., Matsumoto, K. and Yamada, K. M. (2005). A Rac switch regulates random versus directionally persistent cell migration. *J. Cell Biol.* **170**, 793-802. doi:10.1083/jcb.200503152

Paolillo, M. and Schinelli, S. (2017). Integrins and exosomes, a dangerous liaison in cancer progression. *Cancers (Basel)* **9**, 95. doi:10.3390/cancers9080095

Park, S. J., Kim, J. M., Kim, J., Hur, J., Park, S., Kim, K., Shin, H.-J. and Chwae, Y.-J. (2018). Molecular mechanisms of biogenesis of apoptotic exosome-like vesicles and their roles as damage-associated molecular patterns. *Proc. Natl. Acad. Sci. USA* **115**, E11721-E11730. doi:10.1073/pnas.1811432115

Peglion, F., Llense, F. and Etienne-Manneville, S. (2014). Adherens junction treadmilling during collective migration. *Nat. Cell Biol.* **16**, 639-651. doi:10.1038/ ncb2985

Petitjean, L., Reffay, M., Grasland-Mongrain, E., Poujade, M., Ladoux, B., Buguin, A. and Silberzan, P. (2010). Velocity fields in a collectively migrating epithelium. *Biophys. J.* **98**, 1790-1800. doi:10.1016/j.bpj.2010.01.030

Petrie, R. J., Doyle, A. D. and Yamada, K. M. (2009). Random versus directionally persistent cell migration. *Nat. Rev. Mol. Cell Biol.* **10**, 538-549. doi:10.1038/ nrm2729

Peyret, G., Mueller, R., d'Alessandro, J., Begnaud, S., Marcq, P., Mège, R.-M., Yeomans, J. M., Doostmohammadi, A. and Ladoux, B. (2019). Sustained oscillations of epithelial cell sheets. *Biophys. J.* **117**, 464-478. doi:10.1016/j.bpj. 2019.06.013

Phillips, M. J., Calero, G., Chan, B., Ramachandran, S. and Cerione, R. A. (2008). Effector proteins exert an important influence on the signaling-active state of the small GTPase Cdc42. *J. Biol. Chem.* **283**, 14153-14164. doi:10.1074/jbc. M706271200

Plutoni, C., Bazellieres, E., Le Borgne-Rochet, M., Comunale, F., Brugues, A., Séveno, M., Planchon, D., Thuault, S., Morin, N., Bodin, S. et al. (2016). P-cadherin promotes collective cell migration via a Cdc42-mediated increase in mechanical forces. *J. Cell Biol.* **212**, 199-217. doi:10.1083/jcb.201505105

Poujade, M., Grasland-Mongrain, E., Hertzog, A., Jouanneau, J., Chavrier, P., Ladoux, B., Buguin, A. and Silberzan, P. (2007). Collective migration of an epithelial monolayer in response to a model wound. *Proc. Natl. Acad. Sci. USA* **104**, 15988-15993. doi:10.1073/pnas.0705062104

Raleigh, D. R., Marchiando, A. M., Zhang, Y., Shen, L., Sasaki, H., Wang, Y., Long, M. and Turner, J. R. (2010). Tight junction–associated MARVEL proteins MarvelD3, tricellulin, and occludin have distinct but overlapping functions. *Mol. Biol. Cell* **21**, 1200-1213. doi:10.1091/mbc.e09-08-0734

Riazuddin, S., Ahmed, Z. M., Fanning, A. S., Lagziel, A., Kitajiri, S.-I., Ramzan, K., Khan, S. N., Chattaraj, P., Friedman, P. L., Anderson, J. M. et al. (2006). Tricellulin is a tight-junction protein necessary for hearing. *Am. J. Hum. Genet.* **79**, 1040-1051. doi:10.1086/510022

Ridley, A. J., Paterson, H. F., Johnston, C. L., Diekmann, D. and Hall, A. (1992). The small GTP-binding protein rac regulates growth factor-induced membrane ruffling. *Cell* **70**, 401-410. doi:10.1016/0092-8674(92)90164-8

Rink, J., Ghigo, E., Kalaidzidis, Y. and Zerial, M. (2005). Rab conversion as a mechanism of progression from early to late endosomes. *Cell* **122**, 735-749. doi:10.1016/j.cell.2005.06.043

Ross, J. (2007). Colocalisation analysis tools in ImageJ. *Image Process.* **16**, 1-16.

Rothbauer, U., Zolghadr, K., Tillib, S., Nowak, D., Schermelleh, L., Gahl, A., Backmann, N., Conrath, K., Muyldermans, S., Cardoso, M. C. et al. (2006). Targeting and tracing antigens in live cells with fluorescent nanobodies. *Nat. Methods* **3**, 887-889. doi:10.1038/nmeth953

Rothbauer, U., Zolghadr, K., Muyldermans, S., Schepers, A., Cardoso, M. C. and Leonhardt, H. (2008). A versatile nanotrap for biochemical and functional studies with fluorescent fusion proteins. *Mol. Cell. Proteomics* **7**, 282-289. doi:10.1074/mcp.M700342-MCP200

Sánchez-Pulido, L., Martín-Belmonte, F., Valencia, A. and Alonso, M. A. (2002). MARVEL: a conserved domain involved in membrane apposition events. *Trends Biochem. Sci.* **27**, 599-601. doi:10.1016/S0968-0004(02)02229-6

Scarpa, E., Szabó, A., Bibonne, A., Theveneau, E., Parsons, M. and Mayor, R. (2015). Cadherin switch during EMT in neural crest cells leads to contact inhibition of locomotion via repolarization of forces. *Dev. Cell* **34**, 421-434. doi:10.1016/j. devcel.2015.06.012

Small, J. V., Rottner, K. and Kaverina, I. (1999). Functional design in the actin cytoskeleton. *Curr. Opin. Cell Biol.* **11**, 54-60. doi:10.1016/S0955-0674(99)80007-6

Son, K., Hwang, J., Shin, Y., Kim, H., Lee, C., Ko, J., Sun, D., Kwon, B. S. and Kim, J. (2004). PLP2/A4 interacts with CCR1 and stimulates migration of CCR1-expressing HOS cells. *324*, 768-772.

Sonoda, Y., Warita, M., Suzuki, T., Ozawa, H., Fukuda, Y., Funakoshi-tago, M. and Kasahara, T. (2010). Proteolipid protein 2 is associated with melanoma metastasis. *371-376.*

Stadler, M., Scherzer, M., Walter, S., Holzner, S., Pudelko, K., Riedl, A., Unger, C., Kramer, N., Weil, B., Neesen, J. et al. (2018). Exclusion from spheroid formation identifies loss of essential cell-cell adhesion molecules in colon cancer cells. *Sci. Rep.* **8**, 1151. doi:10.1038/s41598-018-19384-0

Sung, B. H., Ketova, T., Hoshino, D., Zijlstra, A. and Weaver, A. M. (2015). Directional cell movement through tissues is controlled by exosome secretion. *Nat. Commun.* **6**, 7164. doi:10.1038/ncomms8164

Taliana, L., Benezra, M., Greenberg, R. S., Masur, S. K. and Bernstein, A. M. (2005). ZO-1: Lamellipodial localization in a corneal fibroblast wound model. *Investig. Ophthalmol. Vis. Sci.* **46**, 96-103. doi:10.1167/iovs.04-0145

Tang, J. C. Y., Szikra, T., Kozorovitskiy, Y., Teixiera, M., Sabatini, B. L., Roska, B. and Cepko, C. L. (2013). A nanobody-based system using fluorescent proteins as scaffolds for cell-specific gene manipulation. *Cell* **154**, 928-939. doi:10.1016/j.cell.2013.07.021

Theveneau, E. and Mayor, R. (2011). Can mesenchymal cells undergo collective cell migration? The case of the neural crest. *Cell Adh. Migr.* **5**, 490-498. doi:10.4161/cam.5.6.18623

Thielicke, W. and Stamhuis, E. J. (2014). PIVlab – towards user-friendly, affordable and accurate digital particle image velocimetry in MATLAB. *J. Open Res. Softw.* **2**, e30. doi:10.5334/jors.bl

Timms, R. T., Duncan, L. M., Tchasovnikarova, I. A., Antrobus, R., Smith, D. L., Dougan, G., Weekes, M. P. and Lehner, P. J. (2013). Haploid genetic screens identify an essential role for PLP2 in the downregulation of novel plasma membrane targets by viral E3 ubiquitin ligases. *PLoS Pathog.* **9**, e1003772. doi:10.1371/journal.ppat.1003772

Tinevez, J. Y., Perry, N., Schindelin, J., Hoopes, G. M., Reynolds, G. D., Laplantine, E., Bednarek, S. Y., Shorte, S. L. and Eliceiri, K. W. (2017). TrackMate: an open and extensible platform for single-particle tracking. *Methods* **115**, 80-90. doi:10.1016/j.ymeth.2016.09.016

Tornavaca, O., Chia, M., Dufton, N., Almagro, L. O., Conway, D. E., Randi, A. M., Schwartz, M. A., Matter, K. and Balda, M. S. (2015). ZO-1 controls endothelial adherens junctions, cell-cell tension, angiogenesis, and barrier formation. *J. Cell Biol.* **208**, 821-838. doi:10.1083/jcb.201404140

Trajkovic, K., Hsu, C., Chiantia, S., Rajendran, L., Wenzel, D., Wieland, F., Schwille, P., Brügger, B. and Simons, M. (2008). Ceramide triggers budding of exosome vesicles into multivesicular endosomes. *Science (80-.)* **319**, 1244-1247. doi:10.1126/science.1153124

Tuomi, S., Mai, A., Nevo, J., Laine, J. O., Vilkki, V., Öhman, T. J., Gahmberg, C. G., Parker, P. J. and Ivaska, J. (2009). PKCε regulation of an α5 integrin-ZO-1 complex controls lamellae formation in migrating cancer cells. *Sci. Signal.* **2**, 1-16. doi:10.1126/scisignal.2000135

Vedula, S. R. K., Ravasio, A., Lim, C. T. and Ladoux, B. (2013). Collective cell migration: a mechanistic perspective. *Physiology* **28**, 370-379. doi:10.1152/physiol.00033.2013

Verweij, F. J., van Eijndhoven, M. A. J., Hopmans, E. S., Vendrig, T., Wurdinger, T., Cahir-McFarland, E., Kieff, E., Geerts, D., van der Kant, R., Neefjes, J. et al. (2011). LMP1 association with CD63 in endosomes and secretion via exosomes limits constitutive NF-κB activation. *EMBO J.* **30**, 2115-2129. doi:10.1038/emboj.2011.123

Vig, D. K., Hamby, A. E. and Wolgemuth, C. W. (2016). On the quantification of cellular velocity fields. *Biophys. J.* **110**, 1469-1475. doi:10.1016/j.bpj.2016.02.032

Warburton, D., Bernard Weinstein, I., Warburton, D., Kahn, S. M. and Bernard Weinstein, I. (1992). Isolation and characterization of a highly malignant variant of the SW480 Human Colon Cancer Cell Line. *Cancer Res.* **52**, 6840-6847.

Weed, S. A., Karginov, A. V., Schafer, D. A., Weaver, A. M., Kinley, A. W., Cooper, J. A. and Parsons, J. T. (2000). Cortactin localization to sites of actin assembly in lamellipodia requires interactions with F-actin and the Arp2/3 complex. *J. Cell Biol.* **151**, 29-40. doi:10.1083/jcb.151.1.29

Wilson, K., Lewalle, A., Fritzsche, M., Thorogate, R., Duke, T. and Charras, G. (2013). Mechanisms of leading edge protrusion in interstitial migration. *Nat. Commun.* **4**, 2896. doi:10.1038/ncomms3896

Yamaguchi, N., Mizutani, T., Kawabata, K. and Haga, H. (2015). Leader cells regulate collective cell migration via Rac activation in the downstream signaling of integrin β1 and PI3K. *Sci. Rep.* **5**, 1-8.

Yoon, W.-H., Lee, S.-K., Song, K.-S., Kim, J.-S., Kim, T.-D., Li, G., Yun, E.-J., Heo, J.-Y., Jung, Y.-J., Park, J.-I. et al. (2008). The tumorigenic, invasive and metastatic potential of epithelial and round subpopulations of the SW480 human colon cancer cell line. *Mol. Med. Rep.* **1**, 763-768. doi:10.3892/mmr_00000026

You, Y., Shan, Y., Chen, J., Yue, H., You, B., Shi, S., Li, X. and Cao, X. (2015). Matrix metalloproteinase 13-containing exosomes promote nasopharyngeal carcinoma metastasis. *Cancer Sci.* **106**, 1669-1677. doi:10.1111/cas.12818

Zhang, Y., Xu, G., Lee, R. M., Zhu, Z., Wu, J., Liao, S., Zhang, G., Sun, Y., Mogilner, A., Losert, W. et al. (2017a). Collective cell migration has distinct directionality and speed dynamics. *Cell. Mol. Life Sci.* **74**, 3841-3850. doi:10.1007/s00018-017-2553-6

Zhang, H., Deng, T., Liu, R., Bai, M., Zhou, L., Wang, X., Li, S., Wang, X., Yang, H., Li, J. et al. (2017b). Exosome-delivered EGFR regulates liver microenvironment to promote gastric cancer liver metastasis. *Nat. Commun.* **8**, 15016. doi:10.1038/ncomms15016

Zhou, J., Li, G., Zheng, Y., Shen, H.-M., Hu, X., Ming, Q.-L., Huang, C., Li, P. and Gao, N. (2015). A novel autophagy/mitophagy inhibitor liensinine sensitizes breast cancer cells to chemotherapy through DNM1L-mediated mitochondrial fission. *Autophagy* **11**, 1259-1279. doi:10.1080/15548627.2015.1056970

Zigmond, S. H. (1996). Signal transduction and actin filament organization. *Curr. Opin. Cell Biol.* **8**, 66-73. doi:10.1016/S0955-0674(96)80050-0